Coastal Engineering 173 (2022) 104098

Contents lists available at ScienceDirect

Coastal Engineering

journal homepage: www.elsevier.com/locate/coastaleng

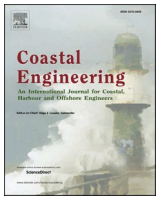

The contribution of hurricane remote ocean forcing to storm surge along the Southeastern U.S. coast

Kyungmin Park [a,*], Ivan Federico [b], Emanuele Di Lorenzo [a], Tal Ezer [c], Kim M. Cobb [d], Nadia Pinardi [e], Giovanni Coppini [b]

[a] Program in Ocean Science and Engineering, Georgia Institute of Technology, Atlanta, GA, USA
[b] Euro-Mediterranean Center on Climate Change, Lecce, Italy
[c] Center for Coastal Physical Oceanography, Old Dominion University, Norfolk, VA, USA
[d] School of Earth and Atmospheric Sciences, Georgia Institute of Technology, Atlanta, GA, USA
[e] Department of Physics and Astronomy, University of Bologna, Bologna, Italy

ARTICLE INFO

Keywords:
Storm surge
Hurricane
Numerical model
Local forcing
Remote forcing
Water level sensor
High resolution

ABSTRACT

The dynamics controlling the spatial and temporal expressions of storm surges over the coastal wetlands and communities of the South Atlantic Bight (SAB) is complex and not well understood. Leveraging a newly developed high-density hyper-local network of water level sensors in the North Georgia coast, we implement and test an unstructured numerical coastal ocean model (up to 10-m horizontal resolution) that can resolve and diagnose the storm-induced sea-level rise during the two Hurricanes Matthew (2016) and Dorian (2019) that have shore-parallel tracks. Using a set of model sensitivity analyses we decompose the drivers of the storm surge into a component that is associated with direct surface forcing by the hurricanes over the targeted area (e.g., local atmospheric wind and pressure condition in the nested model domain) and remote ocean forcing that is connected to hurricane-induced sea level anomalies and baroclinic effect through the open boundary of the model. For both hurricanes, we find that local surface atmospheric forcing leads to a uniform alongshore response in water level along the entire North Georgia coast with amplitudes that are proportional to how close to shore are the hurricane tracks (e.g., stronger in Matthew and weaker in Dorian). However, the alongshore structure and location of maximum storm surge are determined entirely by the arrival timing of ocean remote forcing. In the case of Matthew, the remote forcing arrives within 2 h of the direct passage of the hurricane over North Georgia and drives peak surges in the northern region of the domain (e.g., the City of Savannah and Tybee Island). In contrast, during Dorian, there is a 14-h difference between the remote and local forcing, and maximum storm surges are found in the southern region around Sapelo Island. We estimate that if local and remote forcing were to be simultaneous, the peak storm surge and the water level would be amplified by up to 30% for Matthew and 50% for Dorian. While this sensitivity analysis only includes two hurricanes and is focused on a case study around North Georgia, it is clear that predicting and understanding the regional expressions and timing of the hurricanes' coastal-wide remote ocean forcing in the SAB is important for estimating worst-case scenarios for coastal communities as they face emergency and management decisions.

1. Introduction

The southeastern coast of the U.S. is highly vulnerable to hurricanes, which can lead to loss of life and property damage reaching up to hundreds of billions of dollars for just one hurricane (Grinsted et al., 2019). Storm surge is known as one of the most destructive factors to human life and infrastructure during hurricane events (Shultz et al., 2005; Zhong et al., 2010; Wang et al., 2012; Gayathri et al., 2017). The damages due to storm surge are expected to increase because of sea level rise with more powerful and frequent North Atlantic hurricanes under planetary surface warming (Knutson et al., 2013; Mori and Takemi, 2016; Hoegh-Guldberg et al., 2018). Given the potential threat in the future, better understanding the main drivers that determine storm surges can lead to a more accurate prediction of such catastrophic events, which can in turn help decision makers to manage hurricane-induced risks.

* Corresponding author.
E-mail address: kmpark0616@gatech.edu (K. Park).

https://doi.org/10.1016/j.coastaleng.2022.104098
Received 7 October 2021; Received in revised form 2 February 2022; Accepted 12 February 2022
Available online 16 February 2022

Numerical models are now capable of capturing complex high-resolution physical processes and geographical features and thus have been widely used to investigate and predict storm surges during hurricane events. Earlier storm surge modeling efforts focused on capturing the evolution and the location of maximum storm surge, although the simulations were limited to the coast because of low computational capability, which exclude the coastal dynamic connected with inland flow. In particular, as the water flow from the coast to inland were ignored in the simulations, the modelled storm surges were often overestimated (Gayathri et al., 2017). With the increase of computing resources more advanced models now explicitly consider the geomorphology and the coastal habitats and inland waters (e.g., wetlands in the case of the U.S. southeastern coast) to simulate extreme water level changes from the open ocean to the inland rivers and the marshes during hurricane events (Olbert et al., 2017; Siverd et al., 2019; Santiago--Collazo et al., 2019). However, as the computational cost of the high-resolution simulation is still not affordable to cover a global- or shelf-scale domain size, limited area models in targeted areas of interest have been used to efficiently represent the complicated coastlines and inland waterways (Trotta et al., 2021) and downscale large-scale models.

The main drivers of storm surge in limited area models (e.g., downscaling models) can be separated into local and remote forcing (Morey et al., 2006; Zhong et al., 2010; Liu et al., 2018; Zhang and Li, 2019; Yang et al., 2020). The local forcing represents atmospheric air-sea fluxes of momentum, heat and water occurring in the coastal model domain while the remote forcing is contained in the signals coming from the lateral boundaries of the coastal region in the form of sea surface height, velocity, temperature and salinity. As the definition of what is attributed to local vs. remote forcing is dependent on the sizes of the downscaling models, hurricane characteristics and the surrounding environments (Zhong et al., 2010; Li et al., 2013), the relative role of the two forcings in storm surge widely vary with cases. Zhong et al. (2010), for instance, examined the relative contribution of local forcing (e.g., wind stress on the surface of a model domain) and remote forcing (e.g., non-tidal sea level on the open ocean boundary) during Hurricane Isabel (2003) that passed landward and made landfall in the west of Chesapeake Bay in the U.S. east coast. The remote forcing generated similar storm surges from the estuary to the upper bay in terms of peak level and timing as long waves with little dissipation and amplification. On the other hand, the storm surges induced by the local forcing had spatial variability, showing significantly larger surges in the upper bay than in the lower bay and spatially varying peak timing. The local and remote forcing also showed the different peak levels and timings of storm surges. The local forcing generally caused higher peak surges than remote forcing inside the bay, showing the difference of up to 0.5 m. While the peak timings for local and remote forcing were similar in the lower bay (e.g., Hampton), the remote forcing caused earlier peak surge than local forcing in the upper bay, showing hours differences. Cho et al. (2012) reported that the water level response to remote forcing during Hurricanes Floyd (1999) and Isabel (2003) were similar in the Chesapeake Bay although the two hurricanes had different hurricane tracks and intensities (e.g., Floyd passed directly over the east of the bay). However, the local forcing caused the dramatic difference in storm surge due to different wind directions between the two hurricanes even though the wind speeds during the two hurricanes were similar (e.g., $\pm$ 4 m/s). Specifically, Hurricane Floyd was followed by the offshore winds that caused a set-down in the Bayhead while the onshore winds of Hurricane Isabel increased the water levels in the upper Bay. Eventually, the peak surges between Floyd and Isabel showed greater than 2 m differences in the Chesapeake Bay due to the different roles of the local forcings. Similarly, Liu et al. (2018) reported that remote forcing is of little importance to the spatial distribution of storm surge in the Zhanjiang coastal area at the inlet of the South China Sea although the remote forcing induced higher storm surge than local forcing. Based on 66 historical hurricanes, they simulated storm surges and categorized the spatial patterns of the storm surges to investigate the spatial influence of local and remote forcing on storm surges. Depending on the patterns of storm surges, the remote forcing caused the averaged peak surge in the range of 0.7–1.4 m while the range of averaged peak surge by the local forcing was 0.2–0.9 m. However, as the local forcing interacted with geographical features such as topography and bathymetry, the local forcing controlled the spatial distribution of storm surges in the study. Sensitivity experiments performed by Ma et al. (2017) pointed out that the local forcing could contribute to peak storm surge by up to 62% during Hurricane Leslie (2012) in Placentia Bay on the southeast coast of Newfoundland in Canada. On the other hand, Yang et al. (2020) showed the effects of remote forcing is dominant in storm surge in Salish Sea while the contribution of local forcing to storm surge is about 20% at the peak storm surge and only a few percentages on average during the White Christmas snowstorm (1996) and the Hanukkah Eve windstorm (2006). Taken together, these previous studies show that the effects of local and remote forcing vary widely across coastal areas and are regionally dependent. This implies that the downscaling models are necessary to understand and characterize the storm surge dynamics in specific coastal areas.

The southeastern U.S. coast is highly vulnerable to storm surge damage, however to date, the use of nested 3D high-resolution (~10 m) modeling studies has not been applied comprehensively to understand the drivers of coastal flooding and their relative importance on peak water levels during hurricanes. Previous studies in the southeastern U.S. coast have examined the impact on storm surge from the changes in hurricane's track (Peng et al., 2006; Ezer, 2019), asymmetry (Xie et al., 2011) and forward speed (Thomas et al., 2019). However, the model resolutions used in these studies are relatively coarse (150 m–10 s km) to properly reproduce the complicated coastlines and inland channel networks. In addition to hurricane-induced local forcing such as wind and atmospheric pressure, the variation in coastal sea level can also be affected by a remote forcing such as shelf-scale sea-level anomalies and the Gulf Stream (GS). Morey et al. (2006) reported that local forcing in a downscaling model is not solely responsible for storm surge on the coast during Hurricane Dennis. The remote hurricane forcing, such as barotropic shelf waves, generate a high sea-level anomaly along the coast of West Florida in the U.S. which is amplified by the hurricane winds up to 1 m. Eliot and Pattiaratchi (2010) documented the remote effects generated by the sea-level anomalies along the western side of Australia giving rise to delayed sea level response. Non-isostatic sea level changes (also called non-inverse barometer effects) can contribute to the coastally trapped signals. Zhao et al. (2017) found the non-isostatic oceanic response at frequencies of about 5 days to large-scale atmospheric pressure using bottom pressure data off the continental shelf of the South China Sea and Hong Kong sea level data. The western boundary current, GS, has been also shown to be dynamically linked to coastal sea level along the U.S. east coast (Park and Sweet, 2015; Ezer et al., 2013). Recent studies have reported that the variation in water level is also strongly related to a change in ocean circulation during Hurricanes Matthew and Dorian (Ezer et al., 2017; Ezer 2020). For instance, the GS transport decreased by nearly half during Hurricane Matthew. This weakening and the relaxation of the large-scale sea-level gradient showed a high anti-correlation with an increase in sea level along the U.S. southeast coast (Ezer et al., 2017). Ezer (2020) also reported that a similar weakening of the GS occurred during Hurricane Dorian, which caused elevated coastal sea levels in the days after the hurricane passed the region. Ye at al. (2020) performed a sensitivity experiment to identify the effect driven by GS on water level in the Delaware Bay in U.S. during Hurricane Irene (2011). Their simulation results showed that the storm surge was affected by the change in GS during Hurricane Irene although the effect was not significant. The noticeable effect of the GS on the water level occurred during the post-surge adjustment period that lasted more than 2 weeks. Despite of the importance, the role and contribution of the remote forcing on coastal water level has not been investigated thoroughly along U.S. southeastern coast using

downscaling models.

In this study, we configure a high-resolution downscaling model along the southeastern U.S. coast and inland waterways to investigate the relative role and contribution of local vs. remote drivers on spatial and temporal patterns of storm surge during Hurricanes Matthew (2016) and Dorian (2019). We focus primarily on the North Georgia coast where not only the highest storm surge occurred along the U.S. southeastern coast during the two hurricanes but also a newly developed high-resolution water level sensor network provides an unprecedented observational view of the regional signatures of water level across the coast and wetland boundary. The comparative study of the two hurricanes can provide a unique opportunity to understand mechanisms of observed storm surge as they have coast-parallel tracks that have significant influence on the remote forcing and consequently on the storm surge due to superposition with local forcing (Eliot and Pattiaratchi, 2010). In addition, the two hurricanes show significantly different storm surge effects although they share similar hurricane intensities when they pass southeastern U.S. coast. Therefore, understanding the role of local and remote forcing on storm surge between Hurricanes Matthew and Dorian can provide new insights on hurricane-induced storm surges along the South Atlantic Bight (SAB).

The remainder of the paper is structured as follows. Section 2 describes the characteristics of the two hurricanes and the resultant storm surges from observational evidence. Section 3 provides a description of the numerical model framework and the validation of reproduced total water level and storm surges during Hurricanes Matthew and Dorian. Section 4 illustrates the sensitivity analysis, and section 5 concludes with a discussion.

2. Hurricanes Matthew (2016) and Dorian (2019): description and data

Both Hurricanes Matthew and Dorian were major hurricanes, passing along the southeastern U.S. coast. Hurricane Matthew obtained the name first at 12:00 UTC on September 28, 2016 as the tropical wave developed into a tropical storm near Barbados. Matthew intensified at 00:00 UTC on September 30, increasing its maximum wind from 130 km/h to 270 km/h, which made it Category 5 hurricane on the Saffir-Simpson scale (Stewart, 2017). When the hurricane traveled along the shelf of the SAB, the intensity significantly weakened to a Category 1 hurricane. After Hurricane Matthew made landfall near McClellanville, South Carolina, on October 8, the hurricane pulled away from land toward the northeast until it dissipated on October 10, 2016. The 1-min maximum sustained wind speed and minimum pressure of Matthew were recorded as 270 km/h and 934 mb, respectively (Stewart, 2017). Almost three years later, on August 19, 2019, Hurricane Dorian formed as a tropical wave in western Africa. Dorian was not labeled as a major hurricane until the hurricane hit the U.S. Virgin Islands on August 28, 2019. As the hurricane traveled northward from the U.S. Virgin Islands, a favorable environment rapidly intensified Dorian into a Category 2 hurricane on August 30 and then into a Category 5 hurricane on September 1 with 1-min maximum sustained wind of 295 km/h and minimum pressure of 910 mb (Avila et al., 2019). Dorian made landfall on Grand Bahama at 02:00 UTC on September 2 and stalled in this area for about a day. During the landfall period, the hurricane significantly weakened to a Category 2 hurricane. On September 3, Dorian began to move northward along the warm waters of the GS, making landfall once again in Cape Hatteras, North Carolina as the Category 2 hurricane until it dissipated on September 10 (Avila et al., 2019).

Fig. 1 (a) shows the intensity and tracks of Hurricanes Matthew (square symbols) and Dorian (triangle symbols) with the locations of the center of the hurricanes every 6 h, which are obtained from the National Hurricane Center (NHC). The intensities of the two hurricanes are colored according to the Saffir-Simpson scale. The two hurricanes show a similar hurricane intensity of Category 1 to 3 when they travel along the U.S. southeastern coastline. However, the recorded hurricane damages between Matthew and Dorian were very different. According to reports from the NHC, Hurricane Matthew caused approximately $10 billion in damages, whereas the total damage caused by Dorian was estimated at about $1.6 billion in the United States (Stewart, 2017; Avila et al., 2019). The difference in water level response to the two hurricanes can explain the dramatic difference in damages between Matthew and Dorian. To investigate the water level along the U.S. southeastern coast during the two hurricanes, the five tide gauge stations of the National Oceanic and Atmospheric Administration (NOAA) are selected at Wilmington, North Carolina (NC), Charleston, South Carolina (SC), Fort Pulaski, Georgia (GA), Mayport, Florida (FL1) and Trident Pier, Florida (FL2) as shown in Fig. 1 (a). The maximum nontidal residuals are presented in Fig. 1 (b) to compare hurricane-induced water level between Matthew (blue bar) and Dorian (red bar). The nontidal residuals were calculated by the difference between observed water level and an astronomical tide prediction from NOAA stations. Note that although a

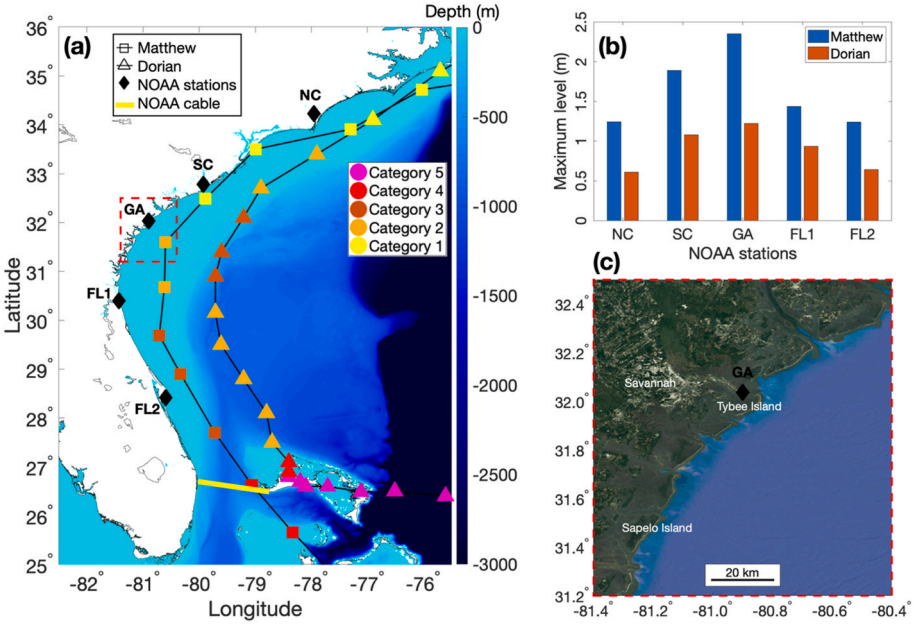

Fig. 1. (a) The location of NOAA tide gauge stations (black diamond), NOAA submarine cable (yellow line) and the hurricane track for Matthew (line with square) and Dorian (line with triangle). The locations of hurricane eyes are indicated every 6 h and the hurricane intensity is colored according to the Saffir-Simpson scale. (b) The maximum nontidal residual at the NOAA stations during Matthew (blue bar) and Dorian (red bar). (c) The targeted area for sensitivity experiments using the limited area numerical model.

storm surge plays a key role in determining the nontidal residual during hurricane event, extreme precipitation, river discharge, wave and tide-surge interaction (TSI) also influence the residual (Thomas et al., 2019; Arns et al., 2020; Santiago-Collazo et al., 2019; Idier et al., 2012). All selected stations along the U.S. southeastern coast show higher peak levels of the nontidal residual during Matthew than those for Dorian in Fig. 1 (b). The different peak level of nontidal residual can be attributed to the different distance of the hurricane eyes from the coastline. Dorian was about 90 km further offshore from the coast compared to Matthew, although the intensity of Dorian was stronger than that of Matthew. The nontidal peak water-level recorded at the tide-gauges increased as the hurricanes travel along the coast and reached its maximum in GA (Fig. 1b). After Matthew and Dorian generated the highest nontidal residual (e.g., 2.35 m for Matthew and 1.22 m for Dorian) in GA, the peak level decreased to 1.26 for Matthew and 0.61 for Dorian as it moved to higher latitude (e.g., NC). The detailed location of GA stations is presented in Fig. 1 (c).

The temporal evolution (6-min interval) of the observed water level (blue line), astronomical tide prediction (red line) and nontidal residual (green line) for Hurricanes Matthew and Dorian at selected stations are illustrated in Fig. 2. The tide predictions at the NOAA tide gauges are calculated by harmonic analysis of multiple years record at each station. Although the tidal ranges during Hurricane Dorian were higher than those of Matthew along the coast because of spring tides, the higher water levels were observed during Matthew than those during Dorian due mainly to the nontidal sea level. The extent of the increase in nontidal sea level was smaller for Dorian compared to Matthew. The GA station experienced the biggest temporal variation in the nontidal residual among the stations during both hurricane events. Furthermore, the nontidal residual showed also a tidal periodicity representing the TSI (tidal signal in nontidal residual) for the two hurricane events. Thomas et al. (2019) reported that the TSI decreased the total water level along the SAB during rising or high tide while increased the water level by TSI was observed during a low or falling tide during Matthew. The TSI widely varied with location along the SAB, showing the magnitude of ~0.1 m (near coast) to ~1 m (in the estuary). In particular, the effect of TSI was stronger at GA station than the other stations in Fig. 2, consistent with the analysis of Feng et al. (2016) that shows most conspicuous effects of TSI on water level at GA among the tide gauge stations along the U.S. east coast in the period 1996 to 2014. Considering the significant impacts of the hurricanes on the GA water levels, the Georgia coast indicated in Fig. 1 (c) is targeted to analyze the main drivers of storm surge through a comparative study of the two Hurricanes Matthew and Dorian.

Fig. 3 shows the time history of the hurricane-induced forcing components during Hurricanes Matthew and Dorian at the GA station, representing the dramatic change in wind speed and direction, and atmospheric pressure. The wind direction and speed for Hurricanes Matthew and Dorian were similar to each other before the two hurricanes were close to the Georgia coast (e.g., on October 5 to 7, 2016 for Matthew and on September 2 to 4, 2019 for Dorian), showing the ±3 m/s difference of wind speed in a southward direction. When the two hurricanes hit the Georgia coast (on October 8, 2016 for Matthew and on September 5, 2019 for Dorian), the wind speed reached up to 25 m/s for Matthew and 16 m/s for Dorian. The wind directions also changed to northeasterly wind (toward southwest), pushing more water into the inland along the Savannah River and increasing the water levels (see nontidal residual in Fig. 3). After the two hurricanes passed the GA station, the water levels dramatically decreased up to −0.6 m due to weakening of wind speed and offshore direction of wind-induced transport. The atmospheric pressures for Matthew and Dorian showed noticeable changes, decreasing to minima of 973 mb and 998 mb, respectively. In addition to dramatic variation in local forcing (e.g., wind and atmospheric pressure), the responses of large-scale ocean circulation to hurricanes were conspicuous during Matthew and Dorian. In Fig. 3 the Florida Current (FC) transport observed by NOAA's submarine cable at 27°N (see the location in Fig. 1) is shown to characterize the western boundary current barotropic transport along the U.S. southeastern coast, feeding the Gulf Stream transport before detachment from the coast. This transport is an indicator of the large-scale ocean circulation on the continental slope (Meinen et al., 2010). Substantial weakening of the FC transport was observed for both hurricane events although the timings when the FC begins to decrease were different between Matthew and Dorian as shown in Fig. 3. During Dorian, the FC

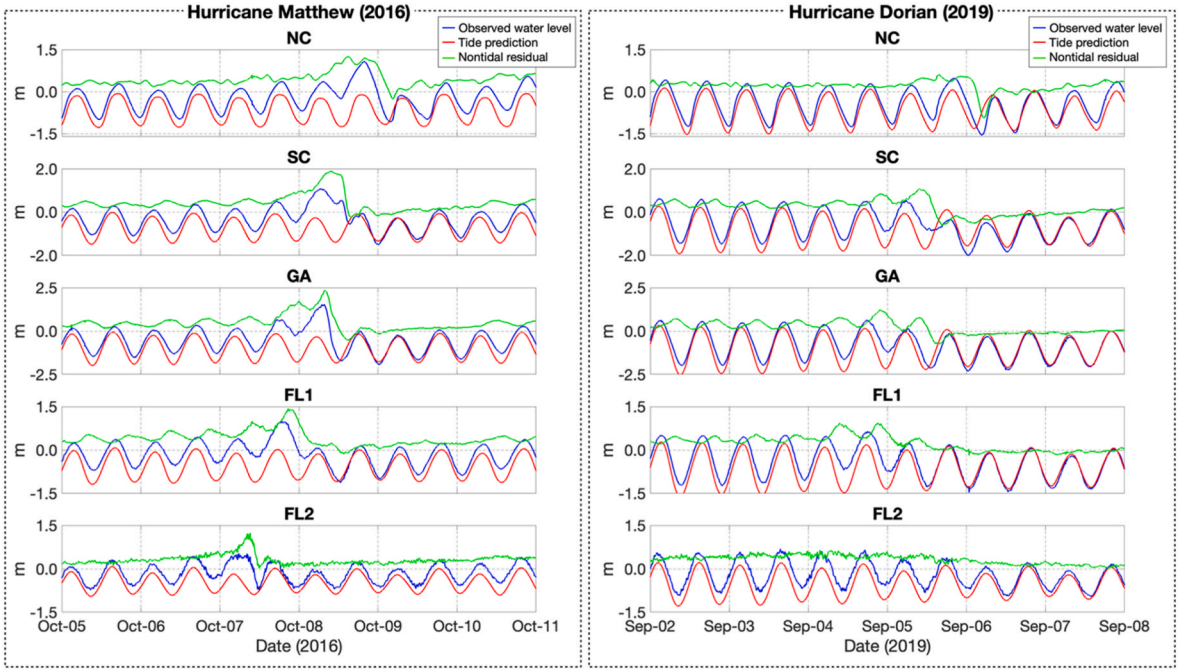

Fig. 2. Time histories of observed water level (blue line) and astronomical NOAA tide prediction (red line) above MHHW for Hurricane Matthew (left column) and Dorian (right column) at five tide gauge stations. The nontidal residual (green line) indicates the difference between the observed water level and astronomical tide prediction.

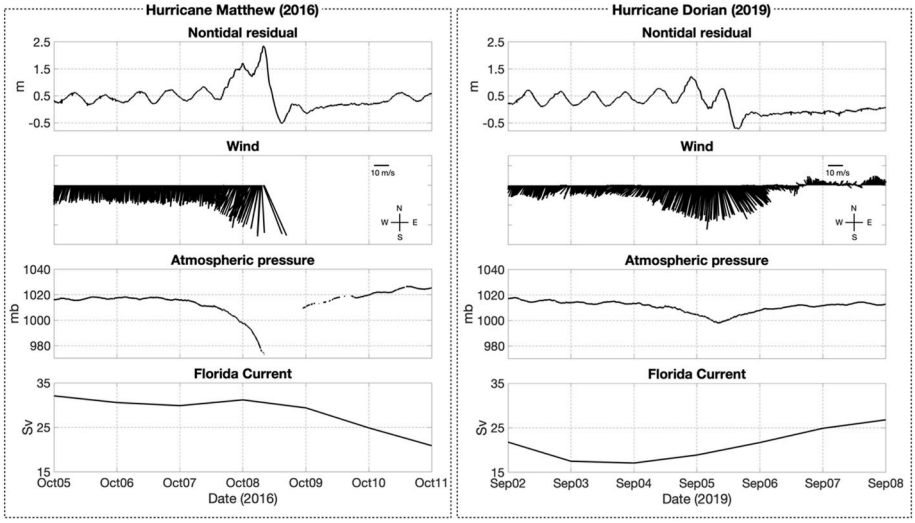

Fig. 3. The temporal evolution of nontidal residual (1st row), wind (2nd row), and atmospheric pressure (3rd row) from the NOAA's Fort Pulaski meteorological station associated with the tide gauge, and the Florida Current transport (4th row) in Sverdrup (Sv) for Hurricanes Matthew (left column) and Dorian (right column).

decreased sharply by about 10 Sv before the maximum storm surge occurred, whereas the intensity of the FC during Matthew was almost constant until Matthew passed the Georgia coast. The FC started to decrease after Hurricane Matthew passes the Georgia coast. Note that the persistence (about 24 h) of Dorian around the Bahama has influenced the different timings of weakening of FC between Matthew and Dorian. The weakening of FC during the hurricane events has been reported to play an important role in water level as remote forcing, showing anti-correlation with coastal sea level along the southeastern U. S. coast (Ezer et al., 2017; Ezer, 2020). The fact that the drop in FC transport during Dorian was earlier than in Matthew meant that when Dorian reached the Georgia coast FC transport had already started to recover and increased which could contribute to lowering sea level and reducing the storm surge impact in Dorian relative to Matthew.

The large-scale footprints of the hurricane sea-level anomalies along the SAB shelf are also an important factor to construct the remote forcing during hurricane events (Morey et al., 2006; Eliot and Pattiaratchi, 2010; Zhao et al., 2017; Zhang and Li, 2019). To better understand the character of the remote ocean forcing in the Georgia coast during the passage of Hurricanes Matthew and Dorian, we decompose the large-scale Sea Surface Height (SSH) evolutions (1-year record) into a High-Pass Filtered (HPF; $\leq$ 11 days) and Low-Pass Filtered (LPF; $>$ 11 days) component for Matthew (in Fig. 4) and Dorian (Fig. 5). The cut-off periods for the filter are decided based on the duration of the two

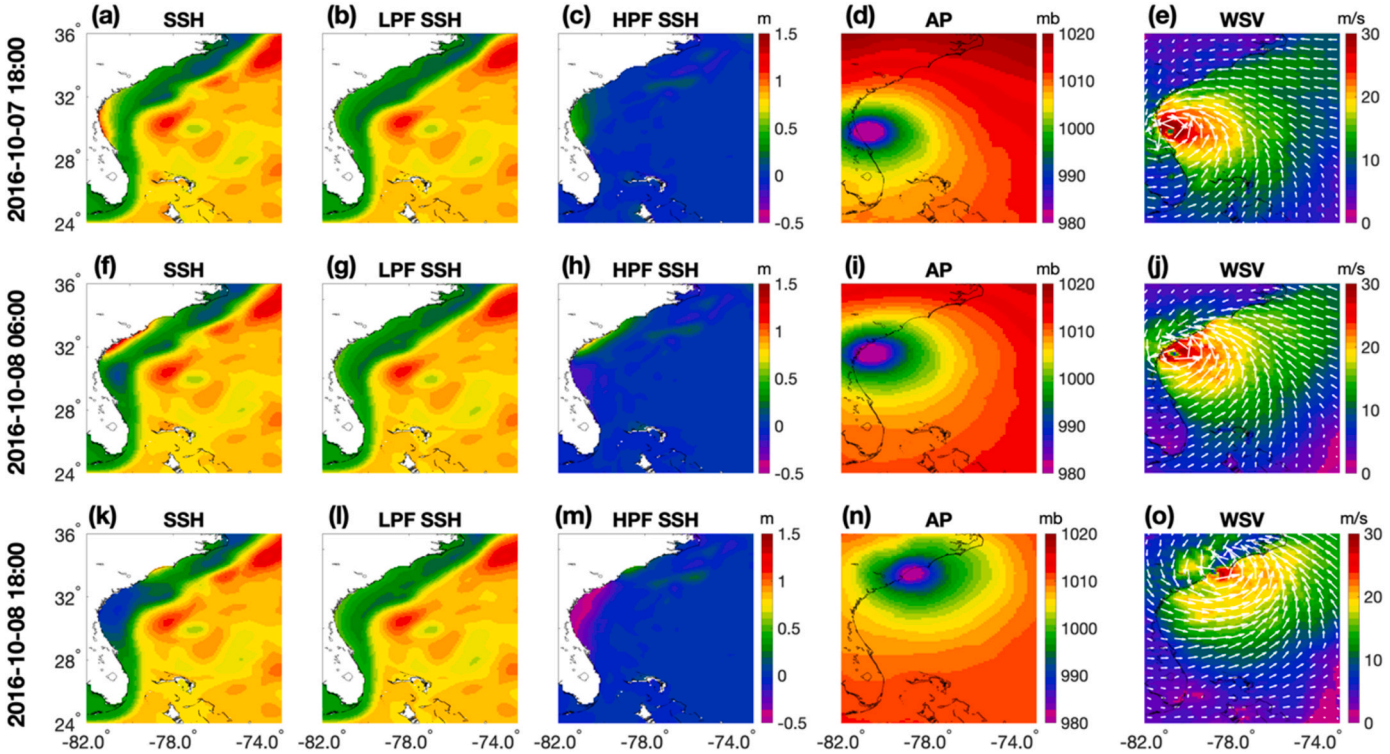

Fig. 4. The instantaneous fields during Hurricane Matthew. Each column from left to right correspond to Sea Surface Hight (SSH), Low-Pass Filtered (LPF) SSH, High-Pass-Filtered (HPF) SSH, atmosphere pressure (AP), wind speed and vector (WSV).

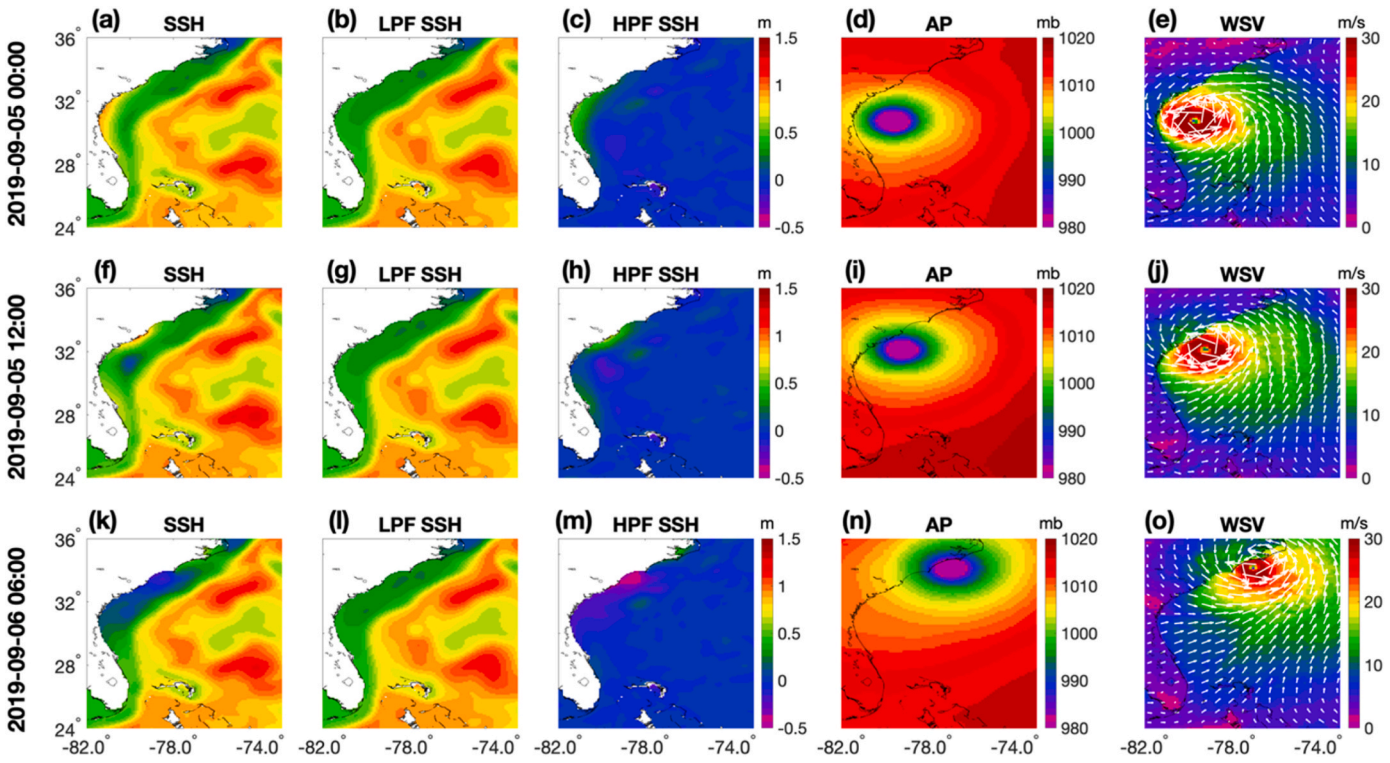

Fig. 5. Same with Fig. 4 but for Hurricane Dorian.

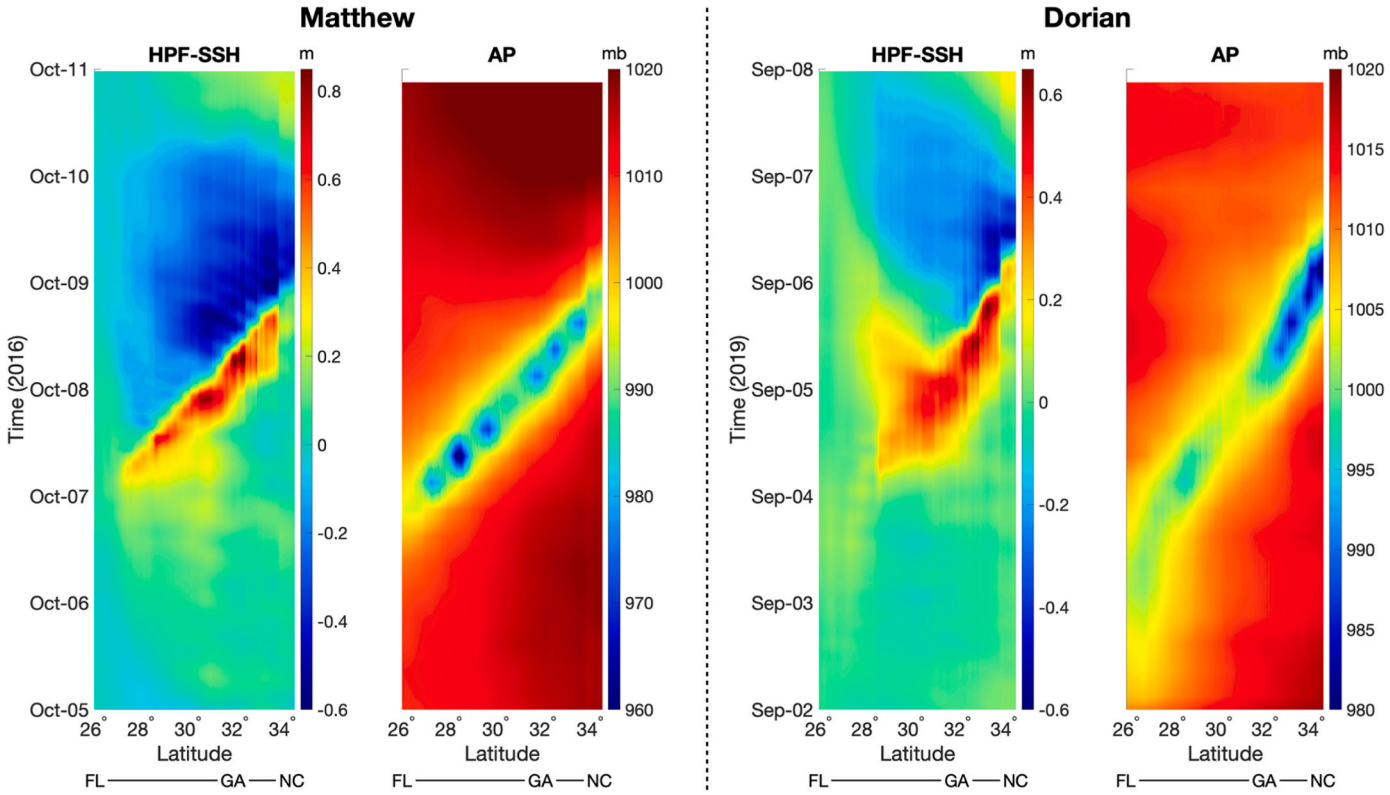

Fig. 6. Hovmöller (latitude-time) diagram of the High-Pass Filtered Sea Surface Height (HPF SSH) and atmospheric pressure (AP) during Hurricanes Matthew (left two columns) and Dorian (right two columns). The latitude in x-axis follows the coastline from Florida (FL) to Georgia (GA) and North Carolina (NC).

hurricanes passing along the SAB. The snapshots in Figs. 4 and 5 show the temporal evolution of SSH, Atmospheric Pressure (AP) and Wind Speed and Vector (WSV) around the Georgia coast. The SSH data is obtained from Copernicus Marine Environmental Monitoring Service's (CMEMS) 1/12 of degree global ocean analysis product while European Centre for Medium-Range Weather Forecasts (ECMWF) analysis products are used for the atmospheric fields. These are the same products used to drive the limited area numerical model presented in section 3. The LPF SSHs show the slow evolving circulation, which by definition changes very slowly during the passage of Matthew and Dorian. In contrast, the responses of HPF SSH clearly show the spatial extent of the oceanic response to the hurricane tracks. The HPF SSH anomalies occur along the coastal boundary at the scale of the entire SAB with higher than usual SSH on the north edge of the hurricanes eye and with lower SSH on the southern edge. The HPF SSH enters the Georgia coast prior to the maximum storm surge.

Hovmöller (latitude-time) diagrams of HPF SSH stretching from the Florida coast to North Carolina in Fig. 6 clearly show the northward propagation of hurricane-induced large-scale SSH anomalies along the SAB shelf, which is connected to coastally amplified anomalies following the hurricane tracks. In particular, hurricanes travelling parallel to the coast (e.g., Matthew and Dorian in this case) have been reported to typically cause most significant impact on coastal sea level compared to other hurricane tracks because the coastally trapped signals can be superposed on local forcing-induced storm surges (Eliot and Pattiaratchi, 2010). We refer to the shelf-scale sea-level anomalies as a factor of remote forcing together with the GS changes in the form of nontidal sea surface height, temperature, salinity and velocity on the open boundary of the model in this study.

This analysis of the large scale, remote forcing conditions during the two hurricane events (Figs. 3–6) already highlight important differences in the temporal evolution of the local response to the remote forcing between Hurricanes Matthew and Dorian. In the case of Matthew, for example, we find larger HPF sea level anomalies than for Dorian. In contrast, earlier weakening of FC occur during Dorian compared with Matthew, implying that the remote forcing caused by the FC/GS large-scale ocean circulation during Dorian can have more influence on water level than Matthew. However, the observations and the large-scale model analysis do not allow a precise understanding of the role and contributions of the local and remote forcing in generating storm surge. Therefore, sensitivity experiments using the limited area numerical model are performed to investigate the effect of different drivers on the storm surge.

3. Numerical model set up

3.1. Model description

SHYFEM is a 3-D fully baroclinic finite element model that solves the Navier-Stokes equations with hydrostatic and Boussinesq approximations (Umgiesser et al., 2004; Federico et al., 2017; Ferrarin et al., 2018). Recent studies have shown that hurricanes also have a significant influence on large-scale ocean circulation (e.g., Gulf Stream on the U.S. east coast) and consequently change the 3-D baroclinic structure of the ocean fields. Specifically, changes in Ekman transport and vertical stratification affect coastal sea level dynamics (Ye et al., 2020; Ezer, 2019). Ye et al. (2020) showed that water levels on the Delaware Bay of the U.S. east coast during Hurricane Irene were better captured by 3-D simulation compared to the 2-D equivalent. For example, the comparison of Gulf Stream transport between 2-D and 3-D simulation showed a mean absolute difference of 19%, which eventually caused differences in the coastal sea level. In particular, the baroclinicity plays a key role in rebounding water level in the post-hurricane period, which can be only captured by 3-D simulation with the baroclinic effect. Therefore, the 3-D simulation is important to properly analyze the effect of hurricanes on coastal sea level, especially in areas where large-scale circulation exists (e.g., Gulf Stream or Kuroshio current). The unstructured grid is Arakawa B with triangular meshes, which is tailored for high-resolution coastal modelling implementations, exploiting its efficiency at handling complex coastlines. Furthermore, the model uses open lateral boundary conditions that smoothly connect the nested area to large-scale and remote processes, fostering the exchange between the different scales. Scalars are computed at grid nodes, whereas velocity vectors are calculated at the center of each element. Vertically a z-layer discretization is applied, and the dynamical variables are averaged over the layers. The vertical discretization in this system has 18 levels. The horizontal resolution ranges from 1 km (open ocean) to 10 m (waterways), allowing an accurate representation of the complex coastlines and channel networks as presented in Fig. 7. The 1/3 arc-second (~10 m) and 3 arc-second (~90 m) resolutions of Digital Elevation Models (DEMs) of NOAA are combined for the model bathymetry. A Total Variation Diminishing (TVD) scheme is applied for horizontal and vertical advection in the transport and diffusion equation for scalars. Horizontal advection of momentum is discretized by an upwind scheme and horizontal eddy viscosity is computed by the Smagorinsky (1963) formulation. For the computation of vertical viscosities and diffusivities, a k–ϵ turbulence scheme is used, adapted from the General Ocean Turbulence Model (GOTM) model described by Burchard and Petersen (1999). At the surface, the air-sea heat flux is parameterized by bulk formulas described by Pettenuzzo et al. (2010), while the surface stress is computed with the wind drag coefficient according to Hellerman and Rosenstein (1983) that calculate the drag coefficient using wind speeds and air-sea temperature differences. The bottom stress is calculated based on quadratic formulation. The bottom drag coefficient in the quadratic formulation is defined by the logarithmic formulation and depends on water depth as specified in Maicu et al. (2021). In the logarithmic formulation, the Von Karman constant and roughness length are constant and equal to 0.4 and 0.01 m, respectively. The model parameters in this study are decided based on previous studies that successfully applied the SHYFEM model in the coastal and inland regions (Ferrarin et al., 2019; Federico et al., 2017; Trotta et al., 2021; Maicu et al., 2021). Although surface waves can significantly contribute to storm surges in coastal areas, the model configuration in this study does not include waves because previous studies show that waves along the Georgia coast play a minor contribution to high water levels and flooding associated with the arrival of hurricanes. Specifically, Marsooli and Lin (2018) show that the maximum wave setup was on the order of magnitude of 10^{-1} m along the U.S east coast during 27 years of historical hurricane events. Near the coast of Georgia, for instance, the maximum wave setup reached near 0.3 m, which is a minor impact of wave setup compared to the large tidal range (e.g., 1.8–2.7 m) on the Georgia coast. Hegermiller et al. (2019) also reported that the wave-current interactions were negligible on the shelf of the U.S. southeast coast during Hurricane Matthew. Consistent these previous findings, the error statistics of the model results (e.g., root mean square error, bias and correlation coefficient) in Table 1 are comparable with or better than other numerical models that include the impact of waves in water levels during Hurricane Matthew (Thomas et al., 2019; Hegermiller et al., 2019). The results show that neglecting waves does not add any significant error in the model results.

The surface forcing, initial and lateral open boundary conditions are interpolated from the CMEMS and ECMWF analysis products. The analysis data provide high accuracy information of past weather and ocean by the data assimilation that combines observations with numerical model results. However, limited spatial and temporal resolutions pose key challenges to properly investigating the coastal sea level. Therefore, the downscaling models (e.g., SHYFEM in this study) using the analysis products play a key role in the assessment of coastal flooding. The CMEMS global ocean analysis products have horizontal resolutions of 1/12° and 50 vertical levels. Dirichlet boundary conditions were employed at the open boundary for sea surface height and inflow active tracers. Total velocities were nudged at the open

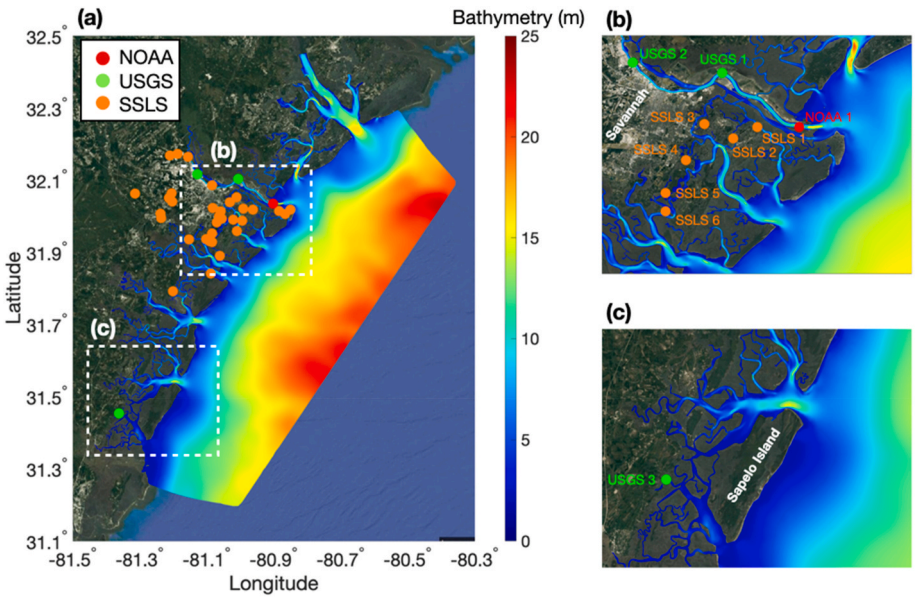

Fig. 7. (a) The model domain with bathymetry in the area of interest, which extend from the open shelf to the inland waterways of Georgia. White boxes indicate specific regions including: (b) the city of Savannah and (c) the Sapelo Island with the locations of observations to compare with model results. The colored dots indicate ten observational stations: one from NOAA (red), three from USGS (green) and six from SSLS (orange).

Table 1
Error statistics of the total water level and storm surge during Matthew and Dorian at different locations indicated in Fig. 7.

Locations	Hurricanes	Total water level			Storm surge		
		RMSE (m)	Bias (m)	R	RMSE (m)	Bias (m)	R
NOAA 1	Matthew	0.212	−0.079	0.958	0.165	0.023	0.930
	Dorian	0.190	−0.013	0.971	0.066	0.012	0.986
USGS 1	Matthew	0.241	−0.108	0.955	0.211	0.023	0.902
	Dorian	0.200	−0.023	0.973	0.083	−0.015	0.963
USGS 2	Matthew	0.334	−0.197	0.937	0.261	−0.018	0.897
	Dorian	0.282	−0.106	0.967	0.097	−0.017	0.968
USGS 3	Matthew	0.241	−0.003	0.934	0.196	−0.012	0.873
	Dorian	0.291	0.045	0.942	0.075	0.016	0.980
SSLS 1	Dorian	0.310	−0.047	0.934	0.096	−0.024	0.984
SSLS 2	Dorian	0.314	−0.037	0.923	0.074	−0.023	0.972
SSLS 3	Dorian	0.366	−0.017	0.901	0.102	0.001	0.979
SSLS 4	Dorian	0.367	0.022	0.911	0.101	0.036	0.976
SSLS 5	Dorian	0.337	0.010	0.914	0.106	0.029	0.972
SSLS 6	Dorian	0.309	0.016	0.931	0.101	0.038	0.975

boundaries and zero gradient boundary conditions were used for outflow active tracers. For initial and open ocean boundary conditions of the SHYFEM model, CMEMS 3-D fields of daily mean water temperature, velocity and salinity are interpolated to horizontal and vertical grids while hourly mean SSHs from CMEMS are utilized to consider the significant and rapid change in the sea levels during a hurricane event. The CMEMS SSH is merged with the tidal astronomical elevations on the ocean open boundaries using fourteen tidal constituents: 2N2, M4, Mf, Mm, Mn4, Ms4, M2, S2, N2, K2, K1, O1, P1 and Q1 from the Oregon State University Tidal Prediction Soft (OTPS) model (Egbert and Erofeeva, 2002). The initial values of temperature and salinity in the regions that are not covered by the CMEMS products (e.g., inland channel and creeks) are extrapolated from the closest coastal nodes of CMEMS using a sea-over-land procedure (Trotta et al., 2021). This method uses a diffusive boundary layer approach that extrapolates the field values on the areas near the coastline where the parent model solutions are not defined. The procedure iteratively computes the ocean quantities on the land grid points, so that these quantities can be interpolated on the nested higher resolution grid. No-slip conditions are applied at closed lateral boundaries (e.g., inland boundaries around rivers and coastlines). The surface forcing is derived from the ECMWF-HRES analysis products with 1/8° horizontal resolution and 6 h of frequency. The ECMWF-HRES product provides information about the atmospheric fields including air temperature, dew point temperature, total cloud cover, mean sea level atmospheric pressure and 10 m wind velocities. In this study, the precipitation and river discharge are excluded. The Matthew and Dorian storm surge simulations are produced by initializing the model four days before the day of highest storm surge, which leads to stable kinetic energy ratios between the currents in the nested domain and the coarse resolution initial condition fields.

3.2. Model validation

Detailed comparison of total water level and storm surge between the model and observations are performed to check the accuracy of the numerical model. The observations used in this study consist of NOAA, USGS and Smart Sea Level Sensors (SSLS) as shown in Fig. 7 (a). As the SSLS have high-density hyper-local network (55 sensors) to observe and record water level around the North Georgia coast, the model results can be evaluated under diverse environments (e.g., inland creeks and wetlands). Ten locations are selected to compare the model results with the observations, which include not only the estuary and the upstream of

rivers but also creeks and salt marshes as shown in Fig. 7 (b) and (c). NOAA 1, USGS 1 and USGS 2 in Fig. 7 (b) are located from the estuary to upstream of the Savannah River while USGS 3 exists on the inland creek around Sapelo Island as shown in Fig. 7 (c). The SSLS 1 to 6 in Fig. 7 (b) represent the observations that measure the water levels in the creeks and the wetlands around the City of Savannah and surrounding Chatham County, GA. Note that the comparisons of model results with SSLS consider only Hurricane Dorian because the SSLSs have recorded the water level since their installation in 2018.

Fig. 8 shows the comparison results of total water level during Hurricane Matthew at the locations of NOAA and USGS stations. Generally, the model can capture well the evolution, peak level and timing of Matthew-induced water levels at most locations. The difference between model and observation is larger in the location upstream of the Savannah River. In particular, the largest differences on the upstream of the river occur after peak level (e.g., near 18:00 UTC on October 8, 2016). We attribute the error at the upstream location to the effect of precipitation and river discharge, which are not resolved in this model. The comparison of model results with USGS 3 around Sapelo Island is also favorable with significant correlations R > 0.9 (see Table 1 for error statistics). Overall, the model shows a good agreement with the available water level observations despite the lack of hydrological forcing and wave, especially when compared with previous model results by Thomas et al. (2019) that used the hydrodynamic model with wave effects to simulate water level along the U.S. southeast during Matthew. The evolution of total water level during Dorian are compared between model and observation in Fig. 9. In this case, we additionally compare the model result with observation in the creeks and wetland using SSLS. As the track of Hurricane Dorian is farther from the coast than that of Matthew and peak storm surges occur around low tide, the maximum water level is not significant during Dorian. However, it is clear that the increased level of low tide (e.g., the water level on September 5 in Fig. 9) and decreased water level after the hurricane passage (e.g., after September 5) show the impact of Dorian on the water level at each observational site. Generally, the model captures the variation induced by Hurricane Dorian and tide at the different locations with significant correlations R > 0.9 (see Table 1).

To better isolate the storm surge signals, we perform a set of simulations without tidal signals at the lateral boundaries. Because the nontidal residual (see Fig. 2) still include the tidal effect (e.g., tide-surge interaction and error of tide prediction; Horsburgh and Wilson, 2007), a data filtering process is utilized to extract pure storm surges from the nontidal residuals (Feng et al., 2016; Spicer et al., 2019; Xiao et al., 2021). This process can be performed by two steps. First, calculate the nontidal residual by subtracting harmonic tidal signals (Pawlowicz et al., 2002) from the observed total water level. Second, extract the storm surge from the nontidal residual using low-pass filter. In this study, we consider a cut-off period of 13 h for the filter based on the tidal characteristics around the Georgia coast (e.g., semidiurnal tide). Figs. 10 and 11 show the comparison of storm surge between the model without tides and the tidally filtered observations during Matthew and Dorian, respectively. The extracted storm surge from observation during Matthew show smoothed evolution unlike modelled storm surge in Fig. 10 because the low-pass filter excludes the rapid increase and decrease in water level by wind direction and speed that have relatively high frequency (see Fig. 2). Therefore, the conspicuous differences in storm surge between model and observation occur in maximum and minimum level. However, the general evolution of storm surge for Matthew is reproduced well by the model, capturing the timing of an increase in storm surge and rebounding water level after the passage of the hurricane (Fig. 10). Unlike Matthew, the storm surge for Dorian develops slowly with a gentle profile. The model can reproduce well not only the timing and magnitude of peak surge but also the entire evolution of storm surge during Dorian (Fig. 11).

To quantitatively evaluate the model results, statistical error parameters are utilized. The root-mean-square error (RMSE) is used to quantify the agreement between observed and simulated water level:

$$RMSE = \sqrt{\frac{1}{N}\sum_{i=1}^{N}(s_i - o_i)^2}$$

where N, o_i and s_i indicate the number of samples, observations and model results, respectively. An ideal value of zero for RMSE means perfect agreement between observed and simulated water level.

The Bias indicates whether the model overestimates (positive value of Bias) or underestimates (negative value of Bias) the observation. Zero Bias means perfect match between model results and observations:

$$Bias = \frac{1}{N}\sum_{i=1}^{N}(s_i - o_i)$$

The correlation coefficient (R) is used to measure the relationship between model results and observation and has values from 0 to 1 where 1 indicate a perfect fit while 0 indicates a complete disagreement:

$$R = \frac{\sum_{i=1}^{N}(s_i - \bar{s})(o_i - \bar{o})}{\sqrt{\sum_{i=1}^{N}(s_i - \bar{s})^2 \sum_{i=1}^{N}(s_i - \bar{s})^2}}$$

These error statistical parameters are calculated for the period of Hurricanes Matthew (October 5 to October 11 in 2016) and Dorian (September 2 to September 8 in 2019). Table 1 shows the error statistical parameters according to observations during Matthew and Dorian. Generally, the RMSE, Bias and R for total water level and storm surge indicate a good agreement with observations at all locations during Matthew and Dorian. The ranges of statistics for the total water level during the two hurricanes are 0.19–0.36 m for RMSE, −0.19 to 0.04 for Bias and 0.91 to 0.96 for R while those for storm surge have 0.07–0.26 m for RMSE, −0.02 to 0.04 m for Bias and 0.89 to 0.98 for R. The errors on

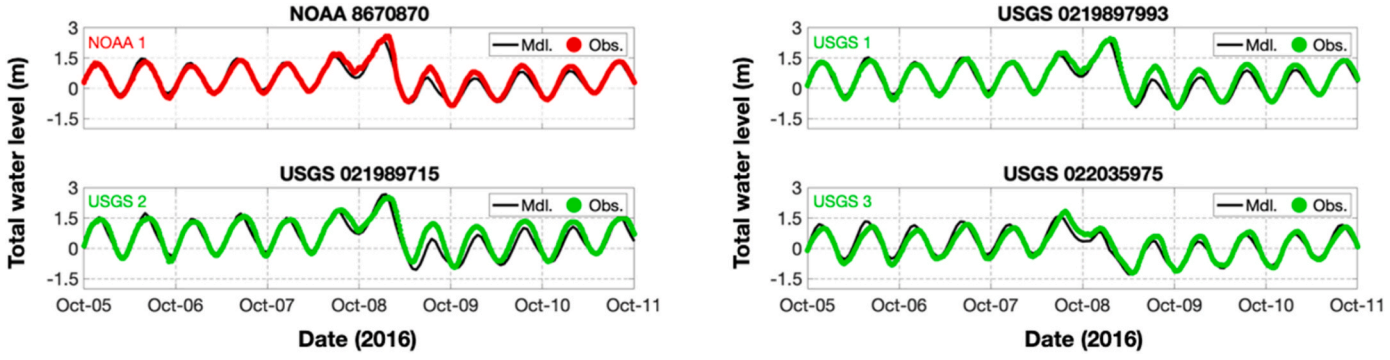

Fig. 8. The comparison of total water level between model and observations during Hurricanes Matthew at different locations (NOAA and USGS) indicated in Fig. 7. Color code is used to indicate the different observations such as NOAA (red) and USGS (green). Here the vertical datum is NAVD88.

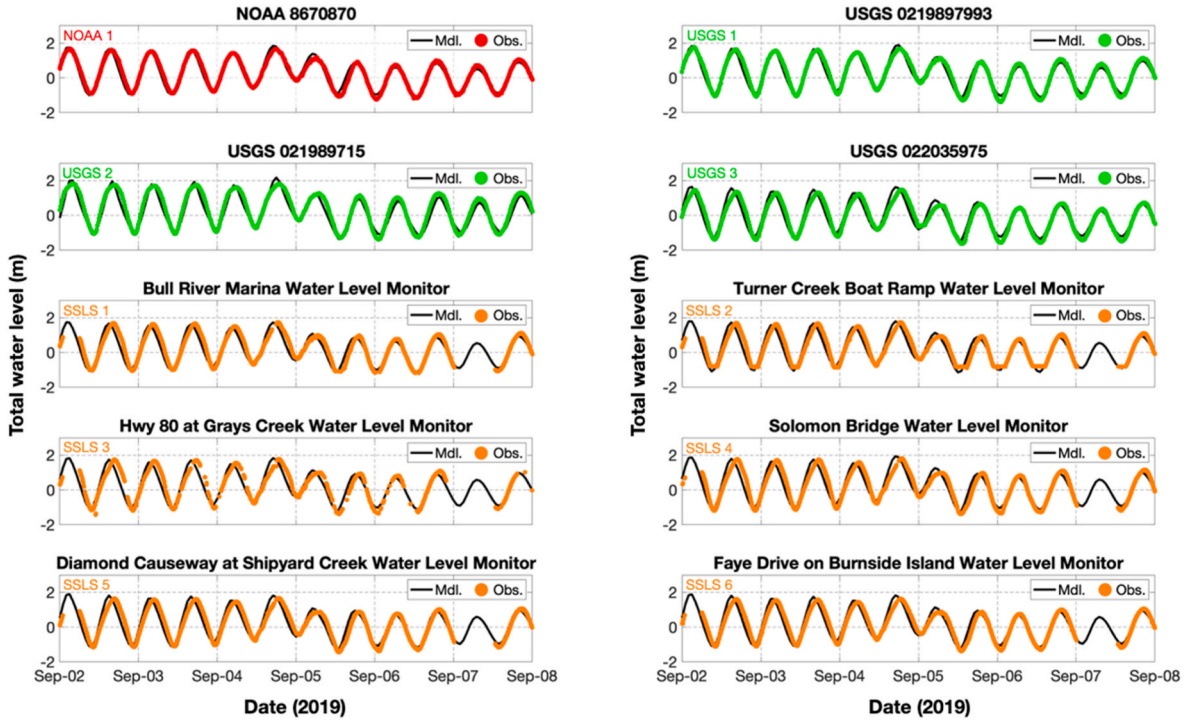

Fig. 9. The comparison of total water level between model and observations during Hurricanes Dorian at different locations indicated in Fig. 7. Color code is used to indicate the different observations such as NOAA (red), USGS (green) and SSLS (orange). Here the vertical datum is NAVD88.

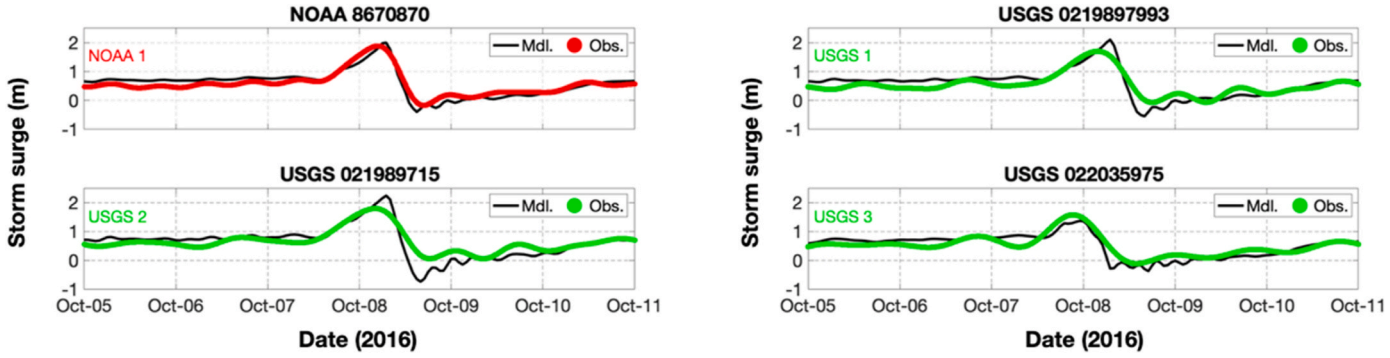

Fig. 10. The comparison of storm surge between model and observations during Hurricanes Matthew at different locations (NOAA and USGS) indicated in Fig. 7. Color code is used to indicate the different observations such as NOAA (red) and USGS (green).

the upstream of Savannah River (USGS 2) and Sapelo island (USGS 3) are relatively large for both Matthew and Dorian, showing higher RMSE (~0.33 m for Matthew and ~0.28 m for Dorian) and lower R (0.93 for Matthew and 0.96 for Dorian). The model underestimates the observed total water level and storm surge on the upstream of the Savannah River, showing the negative Bias for Matthew and Dorian. In wetlands (e.g., the locations of SSLS 1 to 6), the simulated total water level and storm surge during Dorian also show relatively high values of error statistical parameters, which can be caused by interaction with vegetations in the wetlands and small-scale morphology features (small channels and marsh elevations) that are not captured well in DEM or grid systems. Nevertheless, the overall statistics represent a good capability of model to simulate the dynamic change in water levels during the hurricane events, having similar or better error statistics compared to previous studies that utilized hydrodynamics models to simulate the hurricane-induced water level (Thomas et al., 2019; Hegermiller et al., 2019; Zheng et al., 2020). Therefore, within the model errors, we examine the relative role of local and remote forcing in spatial and temporal evolution of storm surge during Hurricanes Matthew and Dorian.

4. Sensitivity experiments

A total of ten sensitivity experiments were conducted to examine the relative role and contribution of different forcing components to the storm surge during Hurricanes Matthew and Dorian. The simulation period of all experiments is 8 days, including spin-up. The simulation for Matthew is carried out from the 4th to the 12th of October in 2016 and denoted as MT, while the time period for Dorian starts on the 1st and ends on the 9th of September in 2019 and it is referred to as DR (see Table 2). As these periods cover extreme water level changes, the experiments help us evaluate the sensitivity of storm surge to local and remote forcing for Hurricanes Matthew and Dorian. The "base simulations" represent the storm surge only simulations without tide and TSI during the hurricane events. The base simulations (BS) that include all forcing are compared with other sensitivity experiments to study the relative contribution of local and remote forcing to the total storm surge. The total storm surge simulations are named as MT-BS and DR-BS for Matthew and Dorian, respectively. The surface forcing (e.g., wind stress and atmospheric pressure) and open ocean boundary conditions (e.g.,

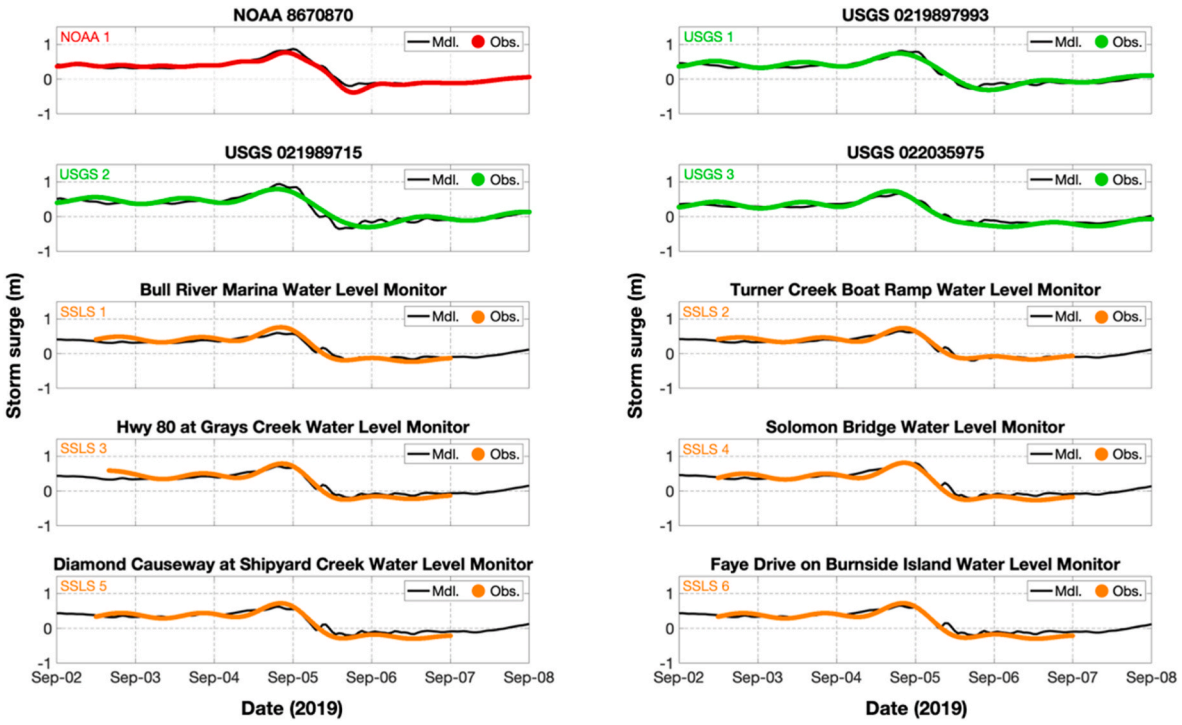

Fig. 11. The comparison of storm surge between model and observations during Hurricanes Dorian at different locations (NOAA, USGS and SSLS) indicated in Fig. 7. Color code is used to indicate the different observations such as NOAA (red), USGS (green) and SSLS (orange).

Table 2
Sensitivity experiments main characteristics. MT = Matthew, DR = Dorian, LF = Local Forcing, RF = Remote Forcing, BS=Base Simulation, WS=Wind Stress, AP = Atmospheric Pressure.

Group index	Experiment name	Description	Simulation period
Base cases	MT-BS	Total storm surge simulation for Matthew	Matthew
	DR-BS	Total storm surge simulation for Dorian	Dorian
Group A	MT-LF	Same as MT-BS but lateral open boundary forcing variability is excluded	Matthew
	MT-RF	Same as MT-BS but local surface forcing is excluded	Matthew
	DR-LF	Same as DR-BS but lateral open boundary forcing variability is excluded	Dorian
	DR-RF	Same as DR-BS but local surface forcing is excluded	Dorian
Group B	MT-WS	Same as MT-LF but the impact of atmospheric pressure is excluded	Matthew
	MT-AP	Same as MT-LF but the impact of wind stress is excluded	Matthew
	DR-WS	Same as DR-LF but the impact of atmospheric pressure is excluded	Dorian
	DR-AP	Same as DR-LF but the impact of wind stress is excluded	Dorian

sea surface height, water temperature, salinity and velocities) are controlled in other experiments to analyze the different forcing components during hurricanes Matthew and Dorian, while other configurations remain the same as that of MT-BS for Matthew and DR-BS for Dorian.

Table 2 summarizes the sensitivity experiments conducted in this study. Since the main drivers during hurricane events are subdivided into Local Forcing (LF) and Remote Forcing (RF), the relative roles and contribution of LF and RF in generating total storm surges are investigated by sensitivity experiments of Group A. The LF consists of Wind Stress (WS) and Atmospheric Pressure (AP) at the surface of the limited area model, whereas the RF represents the adjustment of ocean state to hurricane forcing (e.g., change in Gulf Stream and occurrences of coastally trapped signals) in the form of velocity, salinity, temperature and non-tidal sea-level fluctuation imposed on the open boundary of the model. For the cases of MT-LF and DR-LF in Group A, the nontidal sea-level is specified as zero while, the velocity, salinity and temperature are fixed to their initial values to exclude the impact of the RF variability entering through the open boundaries. For RF experiments (e.g., MT-RF and DR-RF in Group A), the wind speeds are set to zero and atmospheric pressures are kept to a standard atmospheric pressure (1013 mb) over the nested model domain while the open boundary conditions vary with specification of CMEMS fields. The experiments of Group B compare the influences of WS and AP on storm surge to identify their relative role in generating storm surge. As the WS and AP belong to LF, experiments of Group B are based on the configuration of LF cases (e.g., MT-LF and DR-LF) that restrict the impact of RF. In the case of MT-WS and DR-WS, the standard atmospheric pressure is imposed on a surface during the simulation period to ignore the variation in AP by hurricanes, allowing only the impact of WS on storm surge. For MT-AP and DR-AP, the wind stress remains zero to observe how atmospheric pressure affects storm surge, while other parameters remain the same as those of the LF cases.

4.1. Local and remote forcing

In order to investigate the roles of LF and RF in total storm surges over time, the time histories of the storm surge for BS and Group A are compared at Fort Pulaski (e.g., the location of NOAA 1 in Fig. 7) in Fig. 12. The residual (magenta line) in Fig. 12 is calculated by subtracting the sum of LF- and RF-induced storm surge from the total storm surge (e.g., MT-BS and DR-BS), which quantifies an interaction between LF and RF. As the residual in Fig. 12 is close to zero over time at Fort Pulaski, we argue that the interaction between LF- and RF-induced storm surge is negligible and that their combined effects can be modelled as a linear superposition. The LF- and RF-induced storm surges

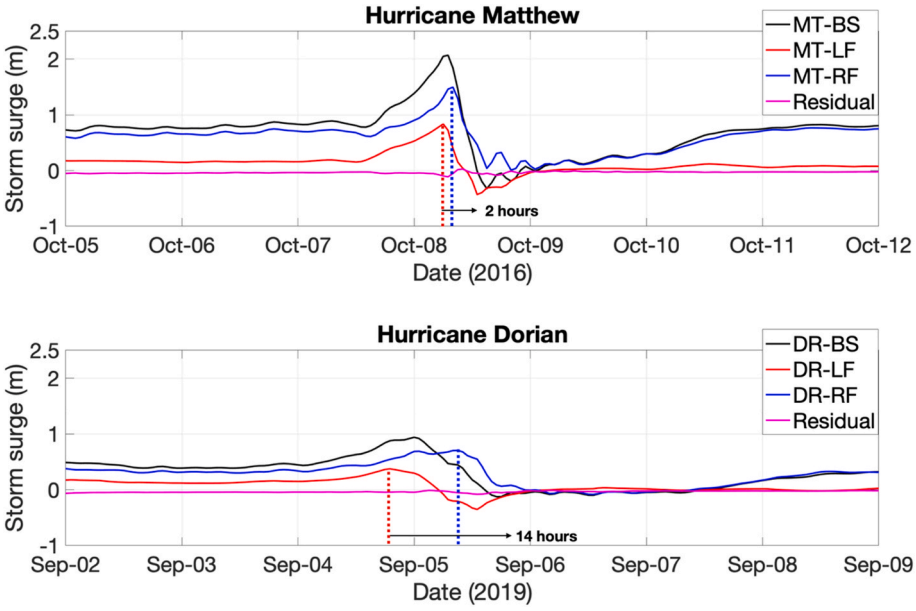

Fig. 12. Temporal variation in storm surge obtained from BS (black line), LF (red line) and RF (blue line) experiments at Fort Pulaski during Hurricanes Matthew (top) and Dorian (bottom). The residual (magenta line) means the difference between storm surge of BS and summation of LF- and RF-induced storm surge. The red and blue dotted lines indicate the arrival timing of peak surge caused by LF and RF, respectively.

for both hurricane events show similar behavior over time. In Fig. 12 the RF-induced storm surges (blue line) for Matthew and Dorian always show higher level than those induced by LF (red line), indicating important role of RF (e.g., coastally trapped signals and Gulf Stream) in generating the total storm surge (black line). As hurricanes approach Fort Pulaski, the LF and RF begin to increase storm surge and reach the peak value within one day. The peak level induced by RF is higher than that of LF by nearly 0.66 m for Matthew and 0.33 m for Dorian. After peak, the LF-induced storm surge for both Hurricanes Matthew and Dorian decreased to negative anomalies when the hurricanes move northeast and the wind shifts from the onshore direction ahead of the storm to offshore in the back of the storm. After Hurricanes Matthew and Dorian pass the North Georgia, the LF-induced storm surge decreases close to zero as hurricane-induced atmospheric forcing disappears. On the other hand, the RF continue to increase the water level again by up to 0.75 m for Matthew and up to 0.3 m for Dorian due to post-hurricane effect of RF ocean adjustment (e.g., baroclinic effect caused by Gulf Stream), which is consistent with previous findings (Ezer 2020; Ye et al., 2020). In summary, the dominant role of RF is identified in the evolution of storm surge over all time including before and after the hurricane events, while the LF mainly contribute to storm surge when Matthew and Dorian are close to targeted area (e.g., Fort Pulaski here). The signs of storm surges for LF depend on wind characteristics while the RF maintains positive anomalies over time at Fort Pulaski during the two hurricanes. The major differences between Matthew and Dorian are found in peak level, timing and duration of storm surge induced by LF and RF. The LF and RF during Matthew result in higher peak storm surge than those of Dorian at Fort Pulaski, showing a difference of 0.46 m in LF-induce peak and 0.79 m in RF-induced peak between Matthew and Dorian. However, the high storm surge effect for Dorian persists longer compared to that of Matthew because Dorian traveled slower than Matthew, which allowed more time for water to converge into the coast. The arrival times of peak surge for LF and RF also show a noticeable difference between Matthew and Dorian as represented with dotted lines in Fig. 12. The peak surge associated with the LF and RF almost occur simultaneously (e.g., 2-h difference) during Hurricane Matthew compared to those of Dorian that show about a 14-h difference in arrival time between LF- and RF-induced peak surge (e.g., LF cause 14-h earlier peak than RF does). Interestingly, the variability of arrival time of locally and remotely induced maximum storm surge can affect the peak timing and level of the total storm surge. For instance, If the RF and LF cause peak surge simultaneously, the maximum total storm surges for Matthew and Dorian increase to about 12.6% and 14.8%, respectively.

The 2-D maps of the maximum storm surges that are the highest surges at each location over the simulation period are presented in Fig. 13 to investigate the spatial influence of LF and RF on the storm surges during hurricanes Matthew and Dorian. The MT-BS and DR-BS in Fig. 13 (a) and (b) represent peak surges including all forcing for Matthew and Dorian, respectively. Note that the open boundary condition of LF simulations seems to restrict the evolution of water level around the lateral boundary as sea-level is imposed to be null on the boundary. However, as the total storm surges at the coast are reproduced well by superposition of LF- and RF-induced storm surge in Fig. 12, we argue that the artificial forcing induced by the open boundary condition in LF experiments does not reach the coast and the inland. We analyze, therefore, the 2-D field of peak surge along the coast, waterways and creeks in this figure. Even if the Matthew and Dorian have similar intensities with shore-parallel track, we can clearly identify some differences in the spatial impacts of LF and RF between the two hurricanes. The LF shows a similar cross-shore gradient of peak storm surge for both hurricanes with lower peak levels on the coast and higher peak levels in the inland where the bathymetry is shallower for both hurricanes. The intensity of the LF pattern is overall larger in Matthew with high peak surges reaching ~1 m along the Savannah River compared to the ~0.5 m during Dorian as presented in Fig. 13 (b) and (f). In contrast, the RFs patterns are characterized by alongshore gradients that are different between Matthew and Dorian. In the case of Matthew, the RF cause higher peak surge in the north region and lower peak value in the south region, and vice versa during Dorian as shown in Fig. 13 (c) and (g). These spatial patterns and magnitudes suggest that the location of peak storm surges along the coast are strongly controlled by the RF, while the LF determines the overall maximum amplitude of water levels in the wetlands (see Fig. 13 (a) and (e)). The RF high sea level was also evident in Figs. 4 and 5 coming from the large scale, global ocean model which however does not reproduce the rich and detailed spatial coastal structure derived by the high-resolution nested model (Fig. 13 versus Figs. 4 and 5). The spatial difference in the peak storm surges between Matthew and Dorian are shown in Fig. 13(i–k) according

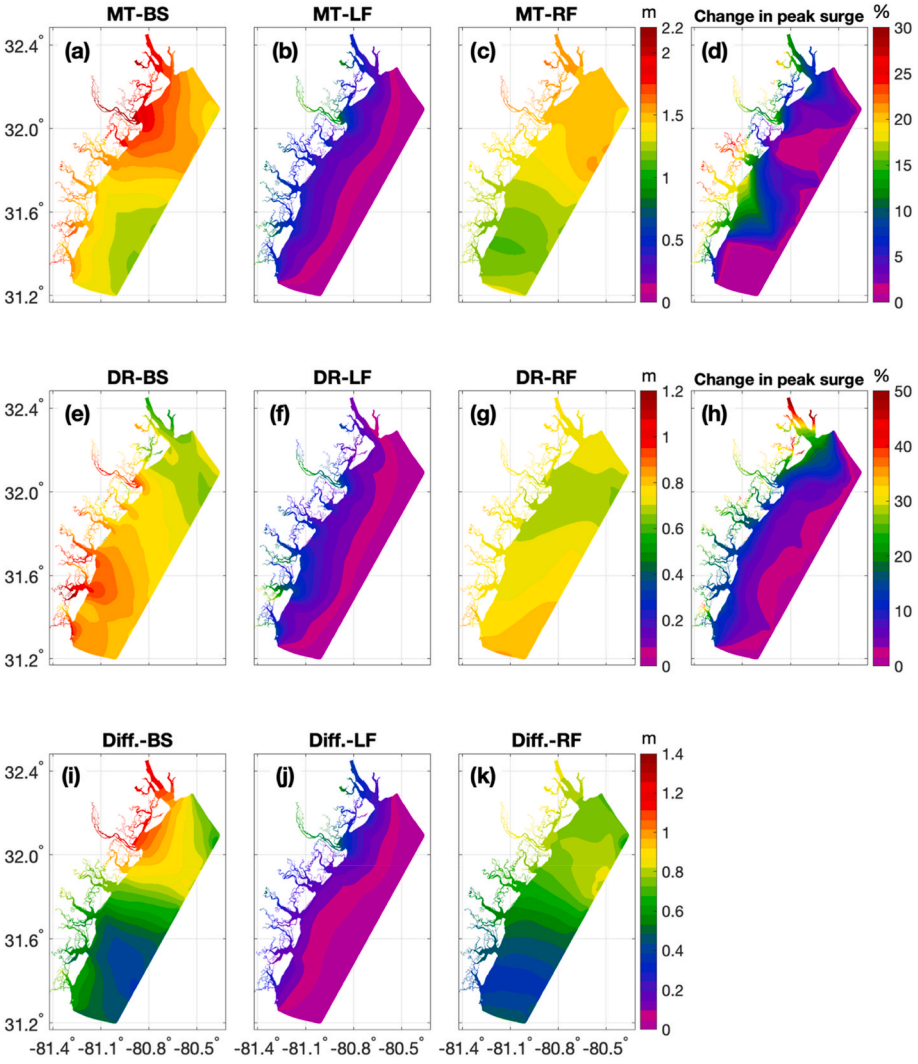

Fig. 13. Maximum storm surge obtained from BS (a and e), LF (b and f) and RF (c and g) experiments for Matthew (first row) and Dorian (second row). The change in peak surge by the aligned peak timings of LF and RF are illustrated in (d) and (h) for Matthew and Dorian, respectively. The differences in peak surge between Matthew and Dorian are presented with regard to BS (i), LF (j) and RF (k) experiments.

to BS, LF and RF experiments. Interestingly, the differences in LF between the two hurricanes are limited to the local area while the RF shows the broader and higher spatial differences. For example, the LF of Matthew causes higher storm surges than those of Dorian mainly along the Savannah River, which amounts to a 0.7 m difference as shown in Fig. 13 (j). On the other hand, in Fig. 13 (k), the spatial differences of RF-induced peak surges between the two hurricanes show evident alongshore gradient that has the small difference of peak level (~0.3 m) in the south region and high difference (~0.9 m) in the north region. Consequently, the RF plays a key role in the different spatial distribution and magnitude of the storm surges in Fig. 13 (i). As the stronger LF and RF of Matthew are concentrated to the north region of the domain, especially around Savannah, the biggest differences in peak surges between Matthew and Dorian occur around Tybee Island and along the Savannah River in Fig. 13 (i), which reaches up to a nearly 1.4 m difference. In contrast, the range of difference in peak storm surge between Matthew and Dorian is from 0.3 m to 0.6 m in the south region of the model domain. The change in maximum surge when the peak surge caused by LF and RF co-occur are presented in Fig. 13 (d) for Matthew and (h) for Dorian. The biggest increase in peak level by the simultaneous peak timings mainly occur in the channel and creeks, showing the increases of up to 30% for Matthew and up to 50% for Dorian. This implies that the variability of peak timing caused by the LF and RF have significant influence on the inland water level compared to those along the coast.

4.2. *Wind stress and atmospheric pressure in LF*

The snapshots of local Wind Stress (WS)- and Atmospheric Pressure (AP)-induced storm surges are illustrated in Fig. 14 to show the spatial influence of WS and AP in the LF response during Matthew and Dorian. The instantaneous fields in Fig. 14 are rendered based on three time slots corresponding to two days before the event day, the event day, and two days after the event day. The event day indicates the time when maximum storm surge occurs at Fort Pulaski during Matthew and Dorian. On the event day, the WS results in a dramatic increase in storm surge up to ~1 m for Matthew and ~0.5 m for Dorian as shown in Fig. 14 (b) and (h). In addition to the different magnitudes of peak surges, spatial patterns of storm surge caused by WS are generally different between Matthew and Dorian. The higher storm surges during Matthew are concentrated in the north region of the model domain, especially around the city of Savannah, while the high storm surges for Dorian occur around both Sapelo Island and Savannah. Although the AP also

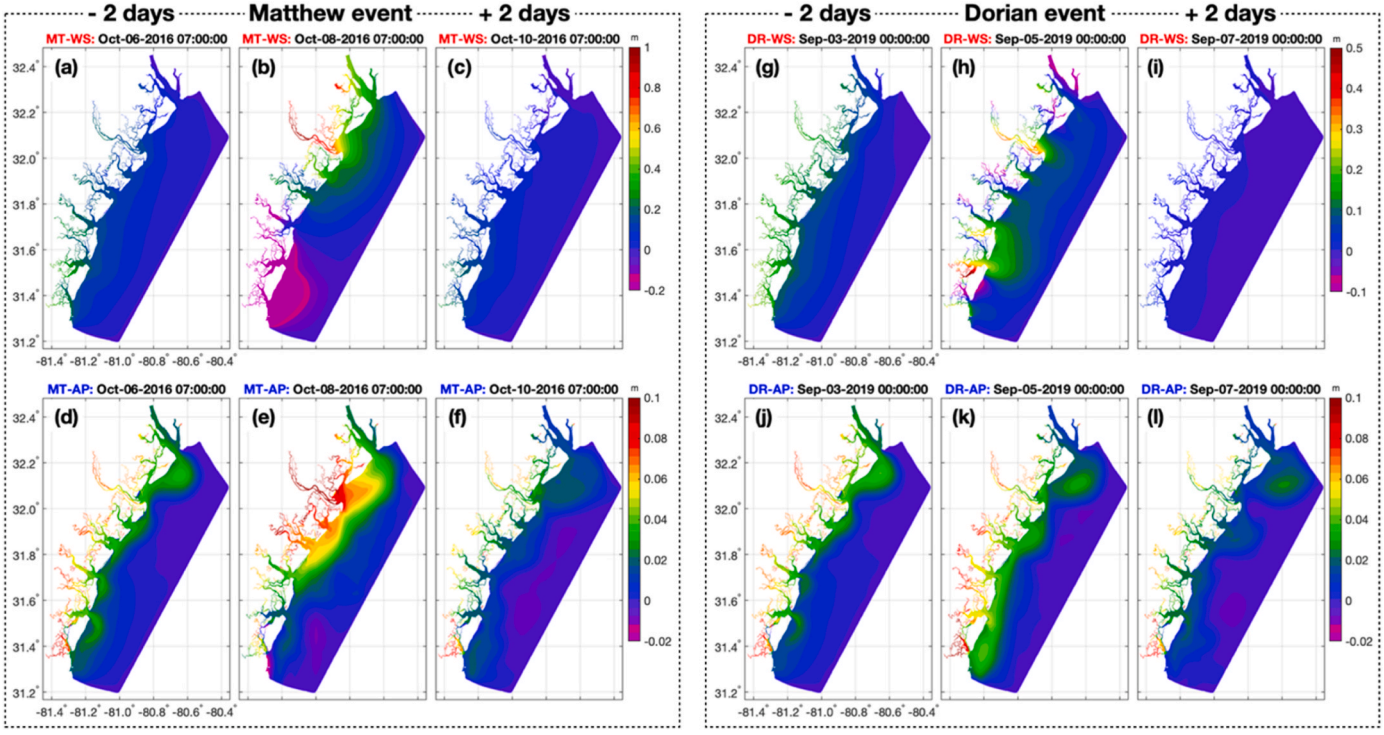

Fig. 14. The instantaneous field of storm surge obtained from WS (first row) and AP (second row) experiments for Hurricanes Matthew (a–f) and Dorian (g–l). Columns correspond to: two days before the storm surge event (first and fourth columns); the storm surge event (second and fifth columns); and two days after the storm surge event (third and sixth columns). The storm surge event here is defined as the time when the peak surge occurs at Fort Pulaski. Note the different color scale for Matthew and Dorian.

causes an increase in storm surge of up to ~0.1 m for Matthew and ~0.08 m for Dorian, the locations where AP-induced storm surge sharply increases on the event day compared to those of two days before are different than those of WS-induced storm surge. For instance, the increased storm surge by AP during Matthew (MT-AP) is observed to spread to the open ocean and south more than those of WS-induced storm surges as compared between Fig. 14 (b) and (e). During Dorian the increase in storm surge by WS (DR-WS) occur around the Savannah and the Sapelo Island as presented in Fig. 14 (h), while the AP of Dorian (DR-AP) causes an increase in the surge mainly along the coast in the south region, especially around the Sapelo Island as shown in Fig. 14 (k). These high-resolution maps show that WS and AP both affect storm surge but with different contributions to the pattern of the surge. The different spatial impacts of WS and AP are attributed to the different mechanisms that lead to the increase in water levels. The low AP around the eye of hurricanes locally pulls up the sea surfaces and increases the

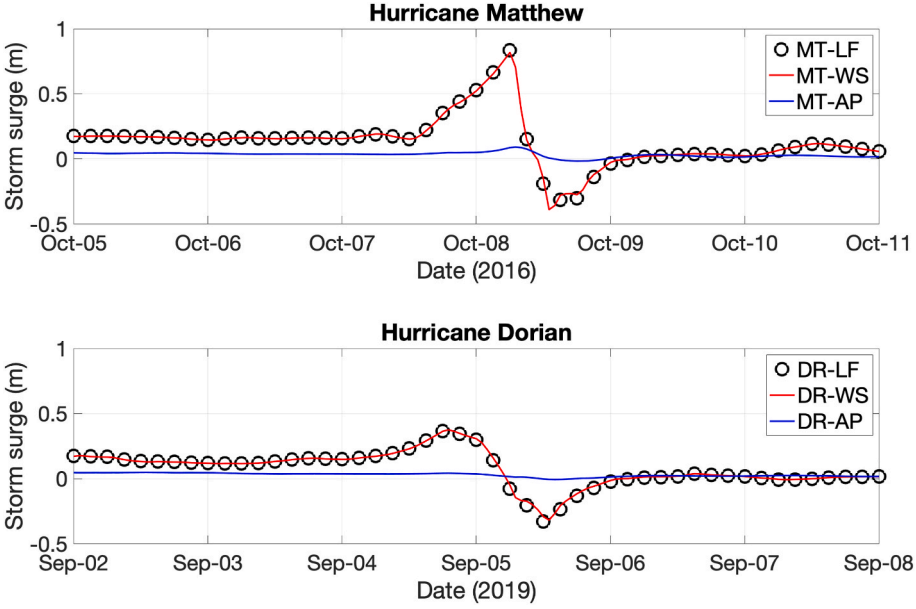

Fig. 15. Temporal variation in storm surge obtained from LF (black circle), WS (red) and AP (blue) experiments at Fort Pulaski during Hurricanes Matthew (top) and Dorian (bottom).

water level. On the other hand, the strength and direction of WS strongly interact with geographical features such as bathymetry and topography to elevate the sea surface. For example, Kennedy et al. (2012) compared the storm surges between steeply-sloping and gently-sloping topographies based on Hurricane Iniki (1992) event and showed the significant increase in surges for the mild-slope topography, which can reach up to 3.5 m higher surge than deeper and steep-sloped bathymetry. The magnitude of AP-induced storm surge is much smaller than that of WS-induced surge, indicating that the storm surge due to AP on the event day accounts for less than 12% of those induced by WS during both Matthew and Dorian. Consequently, it is clear that WS play a dominant role in LF-induced storm surge.

The time histories of the storm surges caused by WS and AP are compared with LF-induced storm surge at Fort Pulaski during Matthew and Dorian in Fig. 15. The profiles of the storm surges caused by WS and LF are almost the same for both Matthew and Dorian, whereas AP-induced storm surge shows only a very minor contribution to the LF-induced storm surge, which again implies the dominant role of WS in LF. Consequently, we attribute the different LF-induced storm surge between Matthew and Dorian to stronger WS of Matthew although both WS and AP of Matthew result in a higher storm surge than those of Dorian.

5. Summary and conclusions

This study reveals the roles of LF (e.g., localized wind and atmospheric pressure over the small subregional areas) and RF (e.g., coastally trapped signals and Gulf Stream) in generating the regional spatial expressions of storm surges and the factors that result in different storm surge responses between two hurricanes that have similar intensities with shore-parallel tracks. A numerical unstructured grid model, SHYFEM, with high-resolution (~10 m horizontal resolution) is utilized to reproduce the storm surges and to investigate their sensitivity in relation to the main drivers that are known to be correlated to the dynamics of coastal sea level. The accuracy and reliability of the model is assessed by the comparison with observation from NOAA, USGS and SSLS – a high-density network of water level sensors for the North Georgia. Through the comparisons and error statistics, it is verified that the model can reproduce well water level changes along the coast, waterways and creeks during Hurricanes Matthew and Dorian.

The high-resolution spatial maps from the SHYFEM model show that the peak storm surges during Matthew and Dorian highly vary with locations along the North Georgia coast, showing the range of peak storm surges from 1 m to 2.2 m during Matthew and from 0.6 m to 1.2 m during Dorian. The details of these regional footprints of peak surge are not captured in the large-scale model and indicate that high-resolution models are needed to properly simulate the spatial variations in extreme water levels. In addition, even if Hurricanes Matthew and Dorian have similar intensities with shore-parallel tracks, the locations in both space and time where peak storm surge occurs are different between the two hurricanes. The LF and RF contributions for Matthew mainly generate high peak surge on the northern region of the model domain whereas the southern region has relatively high level of LF- and RF-induced storm surges during Dorian. The temporal evolution of storm surges caused by the LF and RF indicate the dominant role of RF in generating the high sea levels compared to LF during both hurricane events. In particular, after hurricanes pass the targeted area, the water levels rebound up to 0.75 m for Matthew and 0.3 m for Dorian due to the persistent effect of RF. These simulation results clearly show the importance of properly capturing the basin-scale coastal signals in the downscaling model through the open boundaries of the nested domain. This study also reveals that a key factor to produce the correct storm surge elevation is connected to the arrival times of peak surge induced by LF and RF. For example, if locally and remotely driven peak storm surge were simultaneous, the maximum level in the inland would increase by up to 30% for Matthew and up to 50% for Dorian. We attribute the different role of local and remote forcing between Matthew and Dorian to different distance from the hurricane eye to the targeted area, different ocean adjustments (e.g., coastally trapped signals and large-scale ocean circulation) to the hurricanes and different hurricane size and forward speeds. Note that Hurricanes Matthew and Dorian have shore-parallel tracks passing the U.S. southeast coast so that the two hurricanes can have a persistent influence on the Gulf Stream and coastally trapped signals. Therefore, the relative contributions and roles of LF and RF to the surges can differ if the hurricanes do not have parallel tracks (e.g., landfalling hurricanes). The local forcing that shows the uniform contribution to peak surges (see Fig. 13) along the coast would be also affected by the hurricane tracks. In this first paper we have not fully studied the nature of the remotely forced coastally trapped signals that occur at time frequencies lower than about 11 days from the large-scale atmospheric forcing of the hurricanes. This should be thoroughly investigated in the next paper where experiments could be carried out with larger scale models using different kinds of ocean circulation, atmospheric pressure and wind conditions and analyzing the coastally trapped response.

In addition, we confirm the dominant role of wind stress forcing in LF-induced storm surge through a comparison between storm surges induced by wind and barometric pressure. Specifically, both wind stress and atmospheric pressure generate storm surge during the hurricane, although they drive different patterns and magnitudes of storm surge. However, as the magnitude of the AP-induced storm surge is an order of magnitude smaller than that of the WS-induced surge, the WS alone can represent most of the impact of LF.

Based on these analyses, we attribute the difference in the storm surge effect between Matthew and Dorian on the Georgia coast to not only the stronger LF and RF but also relative timing of the two forcings during Hurricane Matthew. In other words, during Matthew, the similar peak surge timings (e.g., 2-h difference) of LF and RF contribute to a higher peak surge compared to Dorian, which has a 14-h difference between LF- and RF-induced peak storm surges. These finding have important implications for improved and optimized storm surge prediction models which require high-quality, large-scale nesting models and limited area downscaling models, capturing the details of the coastlines and the river estuaries. The knowledge garnered from this study will be able to help evacuation and protection plans based on the characterization of sea level worst-case scenarios.

Finally, while this study explored predominantly the role of LF and RF on sea level change during Hurricanes Mathew and Dorian, we recognize that the compounded effect associated with additional drivers such as extreme precipitation and river discharge become important in the inland areas that are surrounded by marshes and wetlands. Future investigation with the SHYFEM modeling platform that focus on the inland areas, where there is increasing observational data from the hyper-local sensing network provided by SSLS, will include the effects of land-hydrology and precipitation forcing.

Data availability statement

The dataset of NOAA stations used in this study can be downloaded from https://tidesandcurrents.noaa.gov/stationhome.html?id=8670870. The DEMs of NOAA can be obtained from https://www.ncei.noaa.gov/maps/bathymetry/. The CMEMS model data can be obtained from https://resources.marine.copernicus.eu/?option=com_csw&task=results. The ECMWF product can be downloaded from https://www.ecmwf.int/en/forecasts/datasets/catalogue-ecmwf-real-time-products. The sensor data of SSLS can be available from http://bit.ly/cema-portal. The SHYFEM model hindcast and forecast data can be available through http://savannah.cmcc-opa.eu, while the data archive of the sensitivity experiments can be requested by e-mail to corresponding author.

CRediT authorship contribution statement

Kyungmin Park: Methodology, Formal analysis, Validation, Visualization, Investigation, Writing – original draft, Writing – review & editing. **Ivan Federico:** Methodology, Formal analysis, Validation, Writing – review & editing, Funding acquisition. **Emanuele Di Lorenzo:** Project administration, Investigation, Formal analysis, Supervision, Writing – review & editing, Funding acquisition. **Tal Ezer:** Formal analysis, Writing – review & editing, Funding acquisition. **Kim M. Cobb:** Resources, Funding acquisition. **Nadia Pinardi:** Formal analysis, Writing – review & editing. **Giovanni Coppini:** Resources, Funding acquisition.

Declaration of competing interest

The authors declare that they have no known competing financial interests or personal relationships that could have appeared to influence the work reported in this paper.

Acknowledgements

Emanuele Di Lorenzo and Kim Cobb acknowledge the Georgia Smart Communities Sea Level Sensors Grant and Coastal Incentive Grant from the Georgia Department of Natural Resources. The contribution of Ivan Federico and Giovanni Coppini is partially funded by the STREAM (Strategic development of flood management) 2014–2020 European Interreg V-A Italy-Croatia CBC Project.

Appendix. Evaluation of input forcing and boundary conditions

The global-scale models (e.g., CMEMS and ECMWF) are compared with observations to show the uncertainties of input forcing and boundary conditions. In Fig. A.1, the time histories of wind speed and atmospheric pressure from ECMWF analyses are compared with observation at the NOAA station on the Georgia coast (see Fig. 7 for the location). The ECMWF underestimates the peak wind speed (e.g., about 2 m/s difference) and minimum pressure (e.g., about 8 mb difference) during Hurricane Matthew. During Dorian that has a relatively mild hurricane impact, the ECMWF shows better reproduction of atmospheric pressure and wind speed than Matthew although there is still about 2 m/s difference in peak wind speed between ECMWF and observations. The differences are partly due to the spatial and temporal resolution of ECMWF, which cannot capture the dynamic and rapid change in atmospheric fields caused by the hurricanes. Nevertheless, the overall accuracies of ECMWF products are good enough to provide atmospheric forcing input for the SHYFEM model.

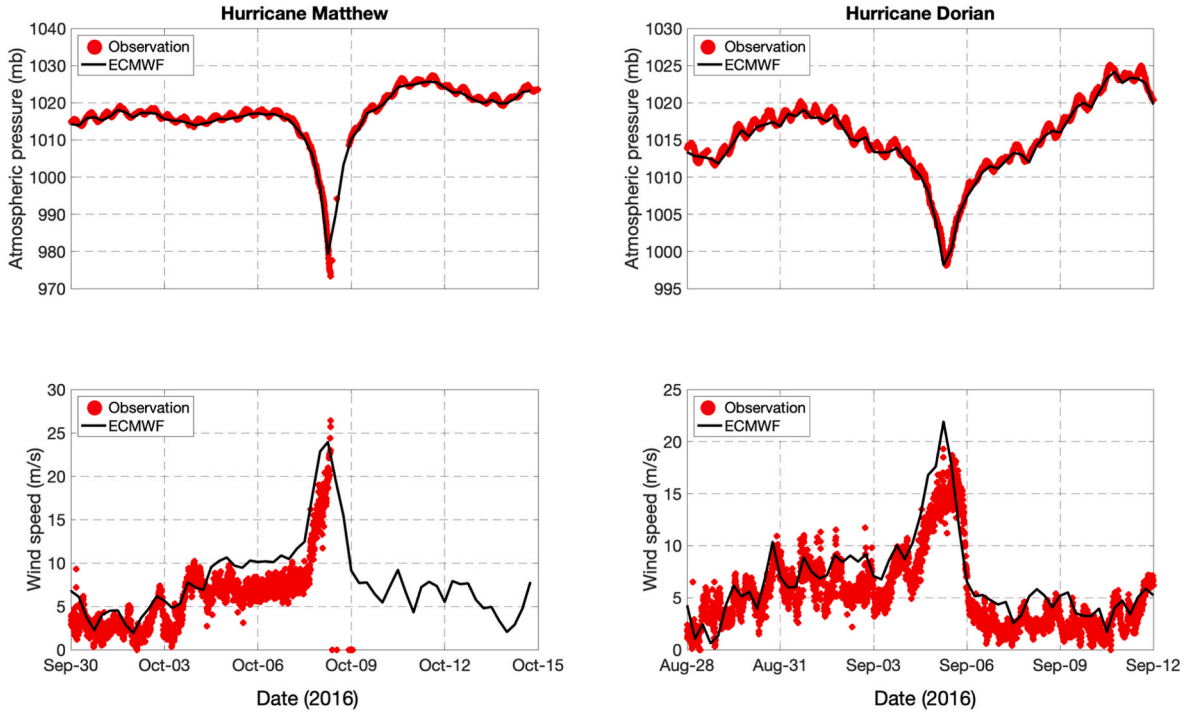

Fig. A.1. The comparison of atmospheric pressure and wind speed between ECMWF and observations for Matthew (left column) and Dorian (right column).

CMEMS products such as 3-D fields of temperature and salinity and SSH also show good agreement with observations (e.g., satellites, tide gauges and Argo). Lellouche et al. (2018) compared the CMEMS's SSH with tide gauges along the U.S. east coast and showed the RMSE of 0.03–0.1 m. For the vertical profile (depth of 0–5000 m) of temperature and salinity, they reported that CMEMS had a global averaged RMSE of about 0.15C^{o} for temperature and about 0.17 psμ for salinity. Because the RMSEs is based on a global scale, we additionally compared the temperature and salinity structure inside the ocean with Argo on the U.S. southeast coast during hurricanes Matthew and Dorian. The locations and identifiers of Argo used in this study are presented in Fig. A.2. Overall comparison results between CMEMS and the observations in Fig. A.3 to A.6 show that the CMEMS captures well the thermohaline structures during the two hurricane events in the U.S. southeast coast. As a result, we utilized the CMEMS product to consider 3-D oceanic forcing (e.g., baroclinic effect) and sea level anomalies coming through the open ocean boundary of the SHYFEM model."

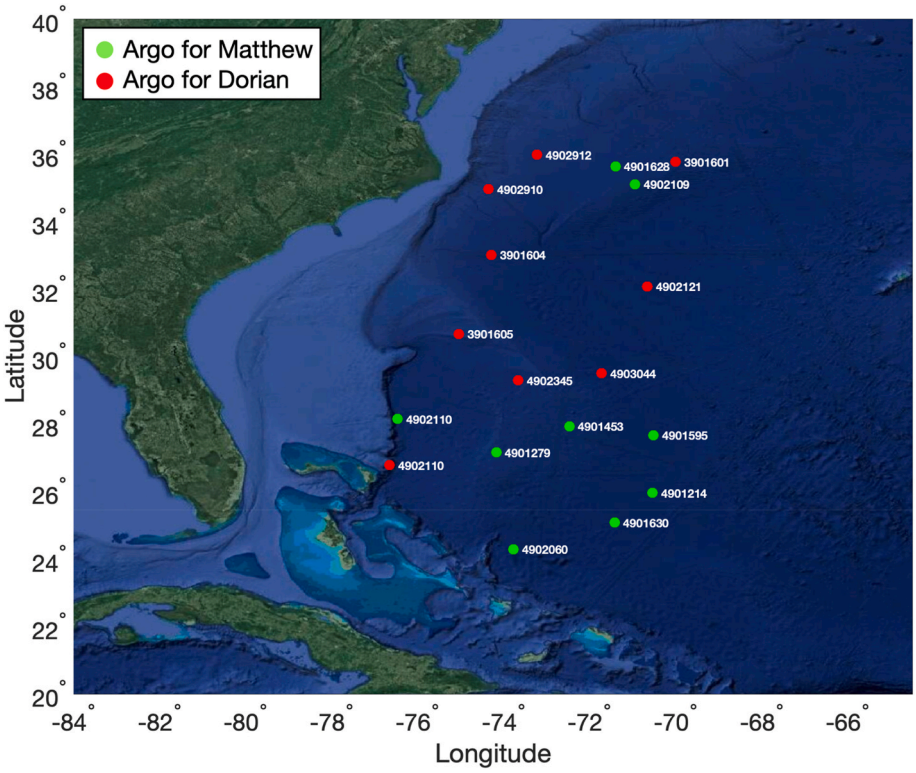

Fig. A.2. The locations and identifiers of Argo profiles for Matthew (green circle) and Dorian (red circle).

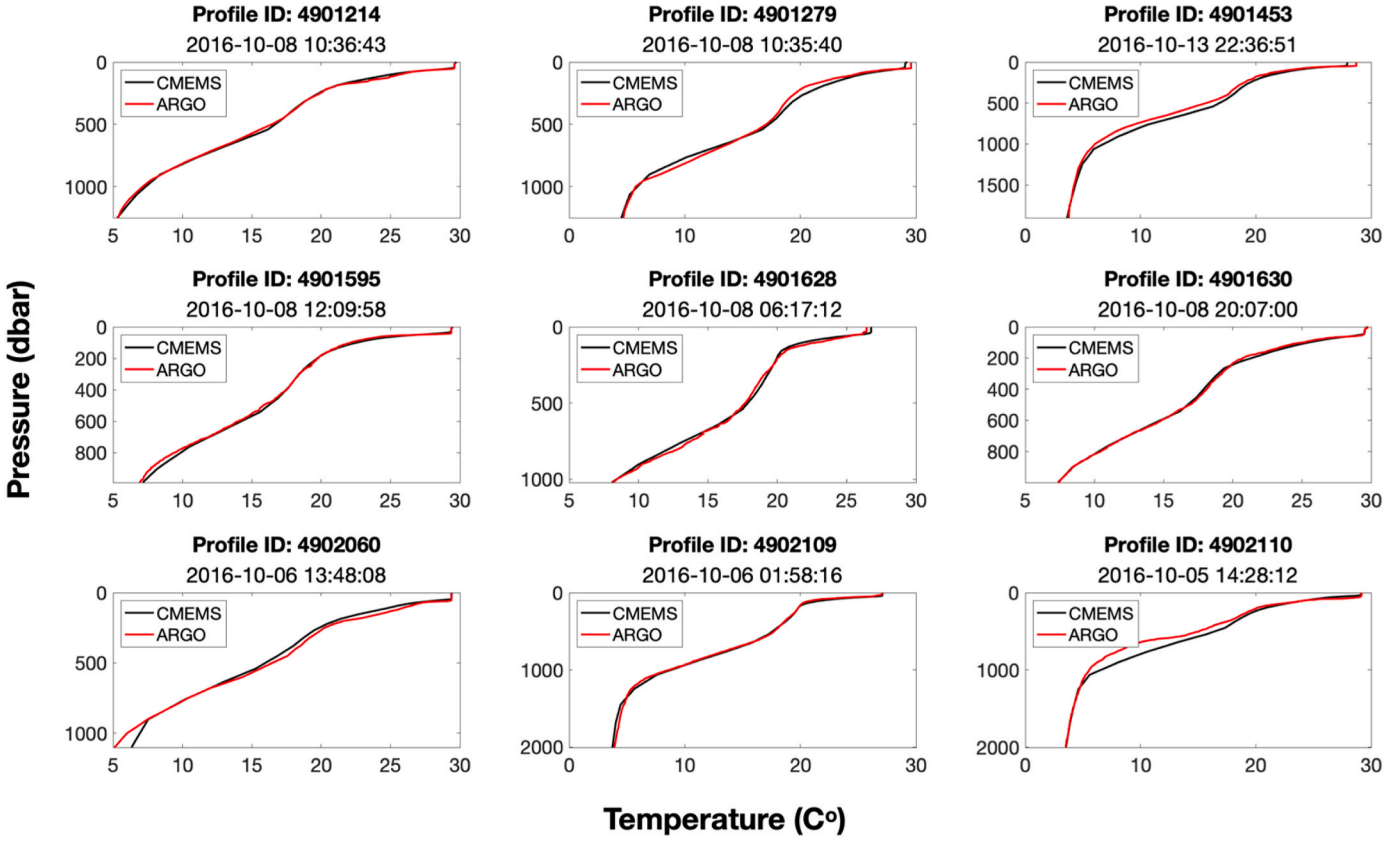

Fig. A.3. Comparison of the CMEMS's temperature with Argo profiles during Hurricane Matthew.

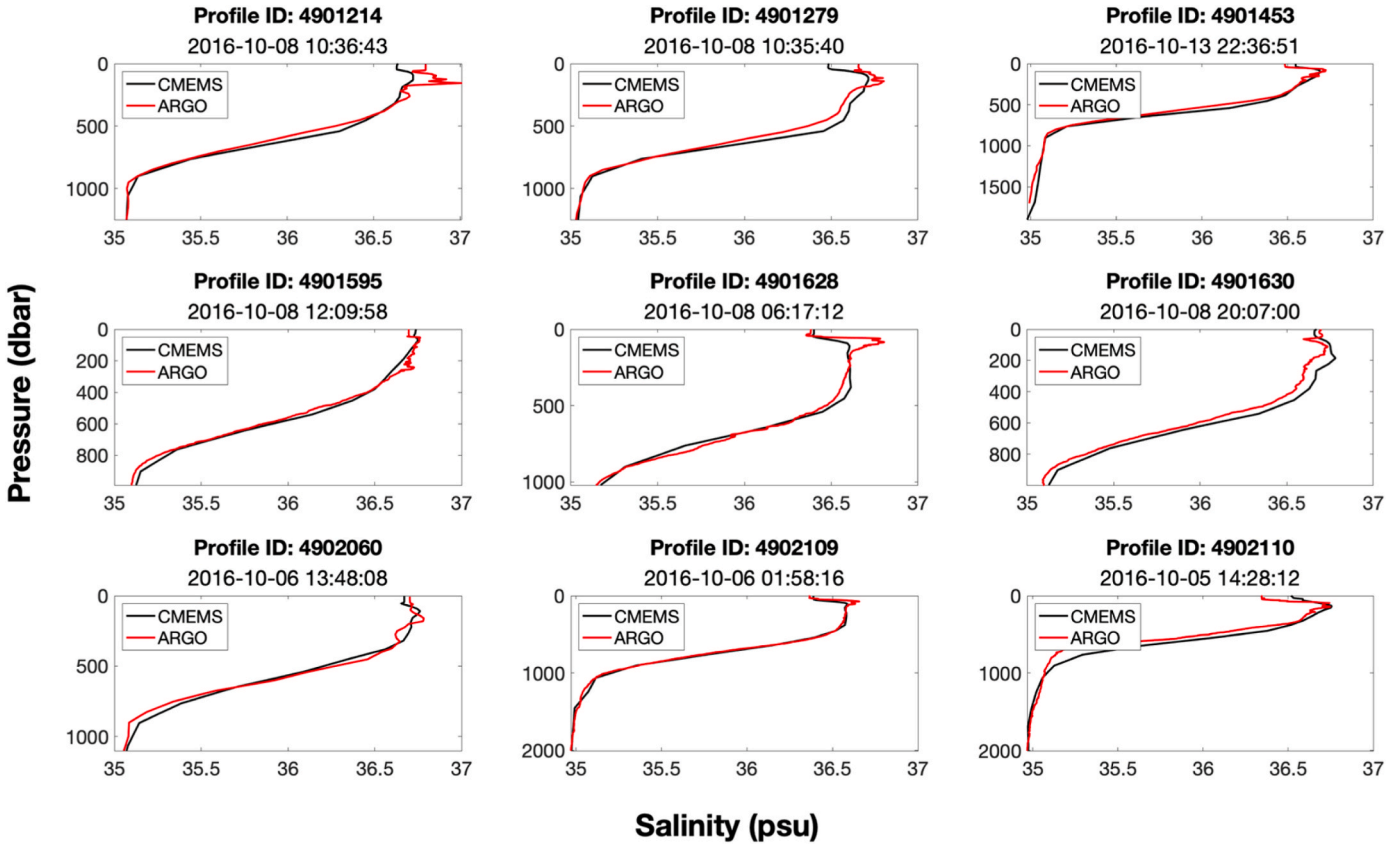

Fig. A.4. Comparison of the CMEMS's salinity with Argo profiles during Hurricane Matthew.

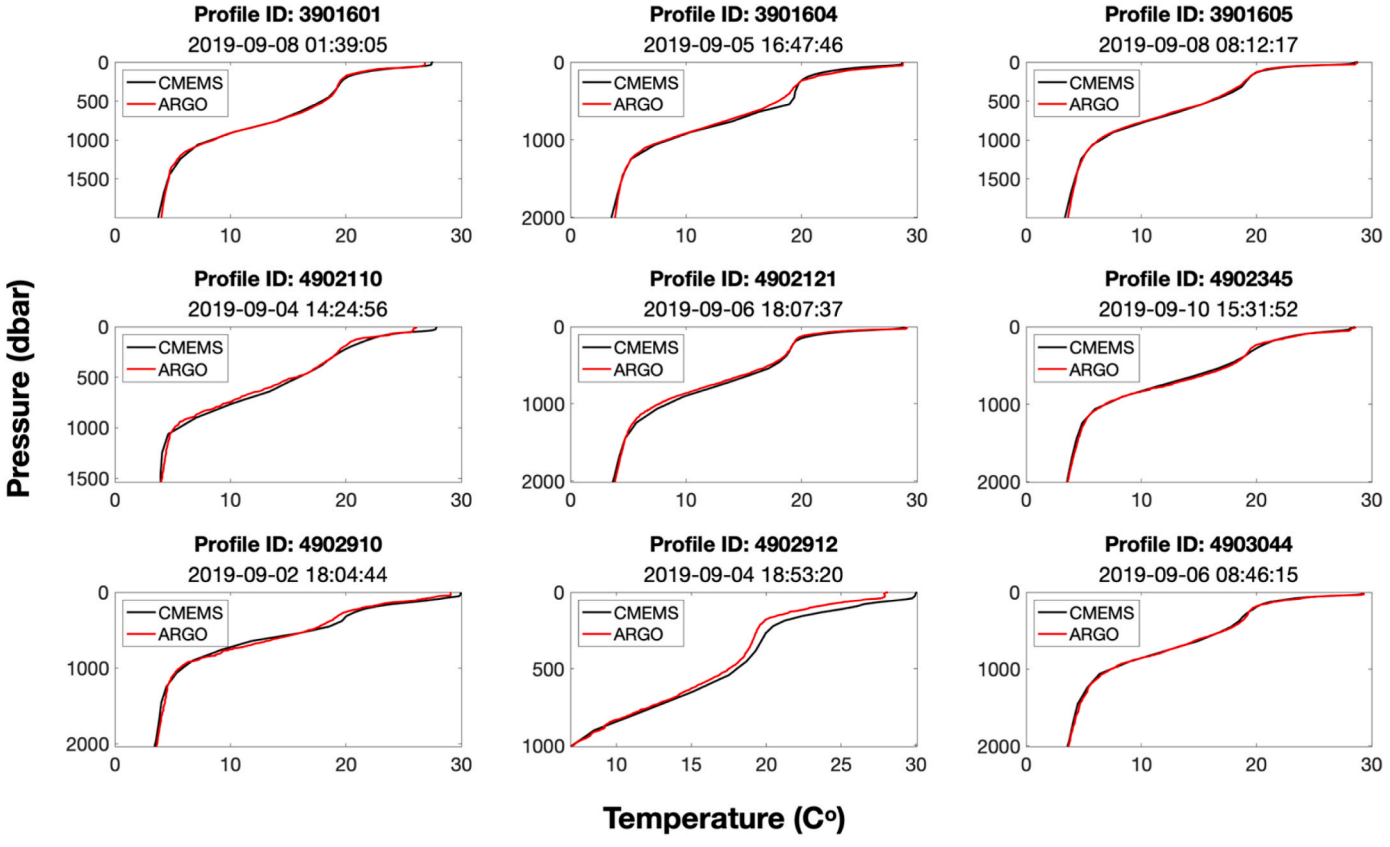

Fig. A.5. Comparison of t the CMEMS's temperature with Argo profiles during Hurricane Dorian.

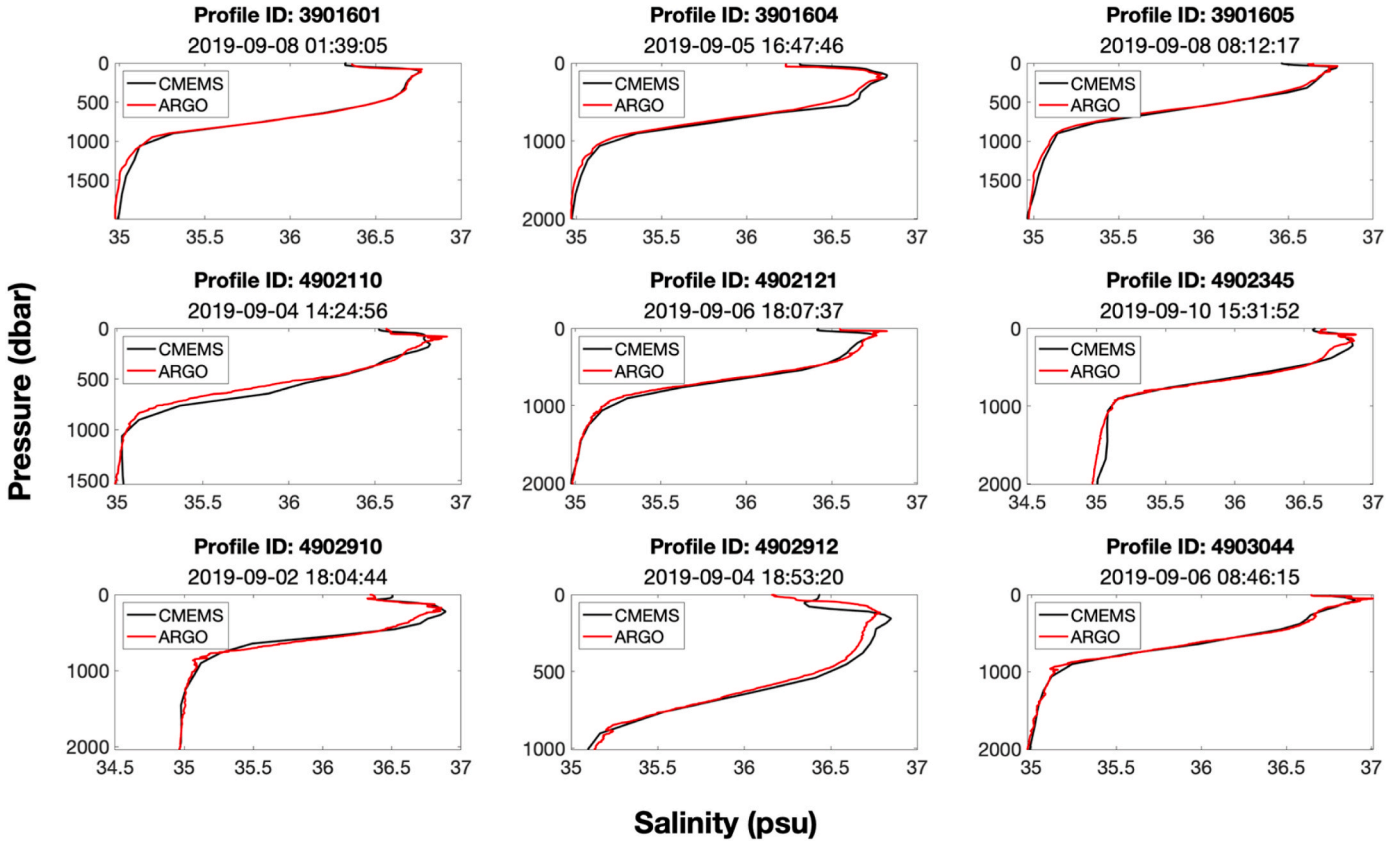

Fig. A.6. Comparison of the CMEMS's salinity with Argo profiles during Hurricane Matthew.

References

Avila, L.A., Stewart, S.R., Berg, R., Hagen, A.B., 2019. Tropical Cyclone Report for Hurricane Dorian (AL052019). National Hurricane Center.

Arns, A., Wahl, T., Wolff, C., Vafeidis, A.T., Haigh, I.D., Woodworth, P., Niehüser, S., Jensen, J., 2020. Non-linear interaction modulates global extreme sea levels, coastal flood exposure, and impacts. Nat. Commun. 11 (1), 1–9. https://doi.org/10.1038/s41467-020-15752-5.

Burchard, H., Petersen, O., 1999. Models of turbulence in the marine environment—a comparative study of two-equation turbulence models. J. Mar. Syst. 21 (1–4), 29–53. https://doi.org/10.1016/S0924-7963(99)00004-4.

Cho, K.H., Wang, H.V., Shen, J., Valle-Levinson, A., Teng, Y.C., 2012. A modeling study on the response of Chesapeake Bay to hurricane events of Floyd and Isabel. Ocean Model. 49, 22–46. https://doi.org/10.1016/j.ocemod.2012.02.005.

Egbert, G.D., Erofeeva, S.Y., 2002. Efficient inverse modeling of barotropic ocean tides. J. Atmos. Ocean. Technol. 19 (2), 183–204. https://doi.org/10.1175/1520-0426(2002)019<0183:EIMOBO>2.0.CO;2.

Eliot, M., Pattiaratchi, C., 2010. Remote forcing of water levels by tropical cyclones in southwest Australia. Continent. Shelf Res. 30 (14), 1549–1561. https://doi.org/10.1016/j.csr.2010.06.002.

Ezer, T., 2019. Numerical modeling of the impact of hurricanes on ocean dynamics: sensitivity of the Gulf Stream response to storm's track. Ocean Dynam. 69 (9), 1053–1066. https://doi.org/10.1007/s10236-019-01289-9.

Ezer, T., 2020. The long-term and far-reaching impact of hurricane Dorian (2019) on the Gulf Stream and the coast. J. Mar. Syst. 103370. https://doi.org/10.1016/j.jmarsys.2020.103370.

Ezer, T., Atkinson, L.P., Tuleya, R., 2017. Observations and operational model simulations reveal the impact of Hurricane Matthew (2016) on the Gulf Stream and coastal sea level. Dynam. Atmos. Oceans 80, 124–138. https://doi.org/10.1016/j.dynatmoce.2017.10.006.

Ezer, T., Atkinson, L.P., Corlett, W.B., Blanco, J.L., 2013. Gulf Stream's induced sea level rise and variability along the US mid-Atlantic coast. J. Geophys. Res.: Oceans 118 (2), 685–697. https://doi.org/10.1002/jgrc.20091.

Feng, X., Olabarrieta, M., Valle-Levinson, A., 2016. Storm-induced semidiurnal perturbations to surges on the US Eastern Seaboard. Continent. Shelf Res. 114, 54–71. https://doi.org/10.1016/j.csr.2015.12.006.

Federico, I., Pinardi, N., Coppini, G., Oddo, P., Lecci, R., Mossa, M., 2017. Coastal ocean forecasting with an unstructured grid model in the southern Adriatic and northern Ionian seas. Nat. Hazards Earth Syst. Sci. 17, 45–59. https://doi.org/10.5194/nhess-17-45-2017.

Ferrarin, C., Bellafiore, D., Sannino, G., Bajo, M., Umgiesser, G., 2018. Tidal dynamics in the inter-connected Mediterranean, Marmara, black and Azov seas. Prog. Oceanogr. 161, 102–115. https://doi.org/10.1016/j.pocean.2018.02.006.

Ferrarin, C., Davolio, S., Bellafiore, D., Ghezzo, M., Maicu, F., Mc Kiver, W., Drofa, O., Umgiesser, G., Bajo, M., De Pascalis, F., Malguzzi, P., 2019. Cross-scale operational oceanography in the Adriatic sea. J. Operat. Oceanogr. 12 (2), 86–103. https://doi.org/10.1080/1755876X.2019.1576275.

Gayathri, R., Bhaskaran, P.K., Jose, F., 2017. Coastal inundation research: an overview of the process. Curr. Sci. 112 (2), 267–278. https://www.jstor.org/stable/24912354.

Grinsted, A., Ditlevsen, P., Christensen, J.H., 2019. Normalized US hurricane damage estimates using area of total destruction, 1900− 2018. Proc. Natl. Acad. Sci. Unit. States Am. 116 (48), 23942–23946. https://doi.org/10.1073/pnas.1912277116.

Hellerman, S., Rosenstein, M., 1983. Normal monthly wind stress over the world ocean with error estimates. J. Phys. Oceanogr. 13 (7), 1093–1104. https://doi.org/10.1175/1520-0485(1983)013<1093:NMWSOT>2.0.CO;2.

Hegermiller, C.A., Warner, J.C., Olabarrieta, M., Sherwood, C.R., 2019. Wave–current interaction between hurricane Matthew wave fields and the Gulf Stream. J. Phys. Oceanogr. 49 (11), 2883–2900. https://doi.org/10.1175/JPO-D-19-0124.1.

Hoegh-Guldberg, O., Jacob, D., Bindi, M., Brown, S., Camilloni, I., Diedhiou, A., Djalante, R., Ebi, K., Engelbrecht, F., Guiot, J., Hijioka, Y., 2018. Impacts of 1.5 C global warming on natural and human systems. In: Global warming of 1.5° C. An IPCC Special Report.

Horsburgh, K.J., Wilson, C., 2007. Tide-surge interaction and its role in the distribution of surge residuals in the North Sea. J. Geophys. Res.: Oceans 112 (C8). https://doi.org/10.1029/2006JC004033.

Idier, D., Dumas, F., Muller, H., 2012. Tide-surge interaction in the English channel. Nat. Hazards Earth Syst. Sci. 12 (12), 3709–3718. https://doi.org/10.5194/nhess-12-3709-2012.

Knutson, T.R., Sirutis, J.J., Vecchi, G.A., Garner, S., Zhao, M., Kim, H.S., Bender, M., Tuleya, R.E., Held, I.M., Villarini, G., 2013. Dynamical downscaling projections of twenty-first-century Atlantic hurricane activity: CMIP3 and CMIP5 model-based scenarios. J. Clim. 26 (17), 6591–6617. https://doi.org/10.1175/JCLI-D-12-00539.1.

Kennedy, A.B., Westerink, J.J., Smith, J.M., Hope, M.E., Hartman, M., Taflanidis, A.A., Tanaka, S., Westerink, H., Cheung, K.F., Smith, T., Hamann, M., 2012. Tropical cyclone inundation potential on the Hawaiian islands of Oahu and Kauai. Ocean Model. 52, 54–68. https://doi.org/10.1016/j.ocemod.2012.04.009.

Liu, X., Jiang, W., Yang, B., Baugh, J., 2018. Numerical study on factors influencing typhoon-induced storm surge distribution in Zhanjiang Harbor. Estuarine. Coast Shelf Sci. 215, 39–51. https://doi.org/10.1016/j.ecss.2018.09.019.

Li, R., Xie, L., Liu, B., Guan, C., 2013. On the sensitivity of hurricane storm surge simulation to domain size. Ocean Model. 67, 1–12. https://doi.org/10.1016/j.ocemod.2013.03.005.

Marsooli, R., Lin, N., 2018. Numerical modeling of historical storm tides and waves and their interactions along the US East and Gulf Coasts. J. Geophys. Res.: Oceans 123 (5), 3844–3874. https://doi.org/10.1029/2017JC013434.

Meinen, C.S., Baringer, M.O., Garcia, R.F., 2010. Florida Current transport variability: an analysis of annual and longer-period signals. Deep Sea Res. Oceanogr. Res. Pap. 57 (7), 835–846. https://doi.org/10.1016/j.dsr.2010.04.001.

Maicu, F., Alessandri, J., Pinardi, N., Verri, G., Umgiesser, G., Lovo, S., Turolla, S., Paccagnella, T., Valentini, A., 2021. Downscaling with an unstructured coastal-ocean model to the Goro lagoon and the Po river Delta Branches. Front. Mar. Sci. https://doi.org/10.3389/fmars.2021.647781.

Ma, Z., Han, G., de Young, B., 2017. Modelling the response of Placentia bay to hurricanes igor and Leslie. Ocean Model. 112, 112–124. https://doi.org/10.1016/j.ocemod.2017.03.002.

Morey, S.L., Baig, S., Bourassa, M.A., Dukhovskoy, D.S., O'Brien, J.J., 2006. Remote forcing contribution to storm-induced sea level rise during Hurricane Dennis. Geophys. Res. Lett. 33 (19) https://doi.org/10.1029/2006GL027021.

Mori, N., Takemi, T., 2016. Impact assessment of coastal hazards due to future changes of tropical cyclones in the North Pacific Ocean. Weather Clim. Extrem. 11, 53–69. https://doi.org/10.1016/j.wace.2015.09.002.

Olbert, A.I., Comer, J., Nash, S., Hartnett, M., 2017. High-resolution multi-scale modelling of coastal flooding due to tides, storm surges and rivers inflows. A Cork City example. Coast Eng. 121, 278–296. https://doi.org/10.1016/j.coastaleng.2016.12.006.

Park, J., Sweet, W., 2015. Accelerated sea level rise and Florida Current transport. Ocean Sci. 11 (4), 607–615. https://doi.org/10.5194/os-11-607-2015.

Peng, M., Xie, L., Pietrafesa, L.J., 2006. A numerical study on hurricane-induced storm surge and inundation in Charleston Harbor, South Carolina. J. Geophys. Res.: Oceans 111 (C8). https://doi.org/10.1029/2004JC002755.

Pawlowicz, R., Beardsley, B., Lentz, S., 2002. Classical tidal harmonic analysis including error estimates in MATLAB using T_TIDE. Comput. Geosci. 28 (8), 929–937. https://doi.org/10.1016/S0098-3004(02)00013-4.

Pettenuzzo, D., Large, W.G., Pinardi, N., 2010. On the corrections of ERA-40 surface flux products consistent with the Mediterranean heat and water budgets and the connection between basin surface total heat flux and NAO. J. Geophys. Res.: Oceans 115 (C6). https://doi.org/10.1029/2009JC005631.

Santiago-Collazo, F.L., Bilskie, M.V., Hagen, S.C., 2019. A comprehensive review of compound inundation models in low-gradient coastal watersheds. Environ. Model. Software vol. 119, 166–181. https://doi.org/10.1016/j.envsoft.2019.06.002.

Siverd, C.G., Hagen, S.C., Bilskie, M.V., Braud, D.H., Gao, S., Peele, R.H., Twilley, R.R., 2019. Assessment of the temporal evolution of storm surge across coastal Louisiana. Coast Eng. 150, 59–78. https://doi.org/10.1016/j.coastaleng.2019.04.010.

Shultz, J.M., Russell, J., Espinel, Z., 2005. Epidemiology of tropical cyclones: the dynamics of disaster, disease, and development. Epidemiol. Rev. 27, 21–35. https://doi.org/10.1093/epirev/mxi011.

Smagorinsky, J., 1963. General circulation experiments with the primitive equations: I. The basic experiment. Mon. Weather Rev. 91 (3), 99–164. https://doi.org/10.1175/1520-0493(1963)091<0099:GCEWTP>2.3.CO;2.

Stewart, S.R., 2017. Tropical Cyclone Report for Hurricane Matthew (AL14202016). National Hurricane Center.

Spicer, P., Huguenard, K., Ross, L., Rickard, L.N., 2019. High-frequency tide-surge-river interaction in Estuaries: causes and implications for coastal flooding. J. Geophys. Res.: Oceans 124 (12), 9517–9530.

Trotta, F., Federico, I., Pinardi, N., Coppini, G., Causio, S., Jansen, E., Iovino, D., Masina, S., 2021. A relocatable ocean modeling platform for downscaling to shelf-coastal areas to support disaster risk reduction. Front. Mar. Sci. 8, 317. https://doi.org/10.3389/fmars.2021.642815.

Thomas, A., Dietrich, J.C., Asher, T.G., Bell, M., Blanton, B.O., Copeland, J.H., Cox, A.T., Dawson, C.N., Fleming, J.G., Luettich, R.A., 2019. Influence of storm timing and forward speed on tides and storm surge during Hurricane Matthew. Ocean Model. 137, 1–19. https://doi.org/10.1016/j.ocemod.2019.03.004.

Umgiesser, G., Canu, D.M., Cucco, A., Solidoro, C., 2004. A finite element model for the Venice lagoon: development, set up, cali- bration and validation. J. Mar. Syst. 51, 123–145. https://doi.org/10.1016/j.jmarsys.2004.05.009.

Wang, J., Gao, W., Xu, S., Yu, L., 2012. Evaluation of the combined risk of sea level rise, land subsidence, and storm surges on the coastal areas of Shanghai, China. Climatic Change 115 (3–4), 537–558. https://doi.org/10.1007/s10584-012-0468-7.

Xie, L., Liu, H., Liu, B., Bao, S., 2011. A numerical study of the effect of hurricane wind asymmetry on storm surge and inundation. Ocean Model. 36 (1–2), 71–79. https://doi.org/10.1016/j.ocemod.2010.10.001.

Xiao, Z., Yang, Z., Wang, T., Sun, N., Wigmosta, M., Judi, D., 2021. Characterizing the non-linear interactions between tide, storm surge, and river flow in the Delaware bay estuary, United States. Front. Mar. Sci. 8. PNNL-SA-162723).

Ye, F., Zhang, Y.J., Yu, H., Sun, W., Moghimi, S., Myers, E., Nunez, K., Zhang, R., Wang, H.V., Roland, A., Martins, K., 2020. Simulating storm surge and compound flooding events with a creek-to-ocean model: importance of baroclinic effects. Ocean Model. 145, 101526. https://doi.org/10.1016/j.ocemod.2019.101526.

Yang, Z., Wang, T., Castrucci, L., Miller, I., 2020. Modeling assessment of storm surge in the Salish Sea. Estuarine. Coast Shelf Sci. 238, 106552. https://doi.org/10.1016/j.ecss.2019.106552.

Zhang, C., Li, C., 2019. Effects of hurricane forward speed and approach angle on storm surges: an idealized numerical experiment. Acta Oceanol. Sin. 38 (7), 48–56. https://doi.org/10.1007/s13131-018-1081-z.

Zhong, L., Li, M., Zhang, D.L., 2010. How do uncertainties in hurricane model forecasts affect storm surge predictions in a semi-enclosed bay? Estuar. Coast Shelf Sci. 90 (2), 61–72. https://doi.org/10.1016/j.ecss.2010.07.001.

Zhao, R., Zhu, X.H., Park, J.H., 2017. Near 5-day nonisostatic response to atmospheric surface pressure and coastal-trapped waves observed in the northern South China Sea. J. Phys. Oceanogr. 47 (9), 2291–2303. https://doi.org/10.1175/JPO-D-17-0013.1.